



저작자표시-비영리-변경금지 2.0 대한민국

이용자는 아래의 조건을 따르는 경우에 한하여 자유롭게

- 이 저작물을 복제, 배포, 전송, 전시, 공연 및 방송할 수 있습니다.

다음과 같은 조건을 따라야 합니다:



저작자표시. 귀하는 원저작자를 표시하여야 합니다.



비영리. 귀하는 이 저작물을 영리 목적으로 이용할 수 없습니다.



변경금지. 귀하는 이 저작물을 개작, 변형 또는 가공할 수 없습니다.

- 귀하는, 이 저작물의 재이용이나 배포의 경우, 이 저작물에 적용된 이용허락조건을 명확하게 나타내어야 합니다.
- 저작권자로부터 별도의 허가를 받으면 이러한 조건들은 적용되지 않습니다.

저작권법에 따른 이용자의 권리는 위의 내용에 의하여 영향을 받지 않습니다.

이것은 [이용허락규약\(Legal Code\)](#)을 이해하기 쉽게 요약한 것입니다.

[Disclaimer](#)

공학박사 학위논문

**Real-time 3D visualization methods
based on dual-dimensional imaging**

이중차원 이미징 기반
실시간 3차원 시각화 방법

2017년 2월

서울대학교 대학원

전기컴퓨터공학부

김 중 현

Abstract

Real-time 3D visualization methods based on dual-dimensional imaging

Jonghyun Kim

Department of Electrical Engineering and Computer Science

College of Engineering

Seoul National University

This dissertation investigates the real-time three-dimensional (3D) visualization method based on light field imaging. Light field imaging is to obtain 3D information in one-shot using a micro lens array in front of the camera sensor. In this dissertation, the 3D information from the light field imaging is reconstructed via integral imaging system in real-time. Based on the base image generation algorithm in multi-view display, the real-time elemental image generation algorithm is proposed for integral imaging. This algorithm can adjust the reconstruction depth plane, so the real 3D images and virtual 3D images can be provided together if needed. The proposed system can visualize real-scale objects in 3D space in real-time, and can be applied to real-time broadcasting technology.

The real-time 3D visualization method can be expanded to light field microscope. The light field information of the micro object obtained from a light field microscope can be reconstructed in 3D via integral imaging system. The elemental image is generated with the similar real-time algorithm, but the

generation should be under the consideration of f-number of the objective lens and that of the display lens array. The proposed method is verified with the implementation of the light field microscope and the integral imaging system. This system can track 3D behavior of the living cells and observe them in 3D and in real-time.

The light field imaging suffers from the limited resolution because of the micro lens array in front of the camera sensor. To overcome this, dual-dimensional imaging method is proposed. A dual-dimensional imaging method is to capture the two-dimensional (2D) and light field images simultaneously using a half-mirror inside the beam path. The obtained 2D and light field images can be upsampled to the high resolution light field based on the Fourier slice photography theorem. The dual-dimensional imaging system is implemented and compared to conventional light field imaging.

The generated upsampled light field is 3D visualized in real-time via a computational light field display. The light field upsampling and the layer image optimization are performed in real-time with the parallel computation. The computational light field display system is implemented by stacking two liquid crystal displays, and can provide the high resolution light field images obtained from dual-dimensional imaging system.

In addition, an elastic micro lens array is fabricated which can be applied to multiple objective lenses in light field microscope. To achieve the maximum resolution in light field microscope, the f-number of the objective lens and that of the micro lens array should be matched, so every objective lens requires paired micro lens array with different f-number. The f-number of the elastic micro lens array can be adjusted by the addressed strength, so the

elastic micro lens array can be paired to multiple objective lenses. By using polydimethylsiloxane (PDMS), the mold of the original micro lens array is obtained. By using the mold, the elastic PDMS micro lens array is fabricated. The elastic micro lens array is verified with a light field microscope system with a 2D stretching device.

Previous 3D display studies mainly have focused on the improvement of viewing characteristics, so the real-time 3D visualization methods have not been discussed much. This dissertation proposes a dual-dimensional imaging method to achieve high resolution light field images in one-shot, and a real-time 3D visualization method via computational light field display systems. The proposed method is expected to be applied in 3D broadcasting technologies and in 3D biomedical technologies.

Keywords: Real-time 3D visualization, light field imaging, light field microscope, f-number matching, elastic micro lens array.

Student Number: 2011-20814

Contents

Abstract	i
Contents	iv
List of Tables	vi
List of Figures	vii
Chapter 1 . Introduction	1
Chapter 2 . F-number matching method using elastic micro lens array in light field microscopy	11
2.1 Introduction.....	11
2.2 F-number variation of elastic micro lens array.....	13
2.2.1 F-number matching problem in light field imaging.....	13
2.2.2 Fabrication of elastic micro lens array with PDMS.....	14
2.2.3 Strain response and F-number variation	16
2.3 F-number matching method using elastic micro lens array	20
2.4 Conclusion	24
Chapter 3 . Real-time 3D visualization method based on light field imaging	25
3.1 Introduction.....	25
3.2 Real-time elemental image generation algorithm.....	28
3.3 Real-time capturing and 3D visualization method based on integral imaging	33
3.4 Real-time integral imaging system for light field microscopy	42
3.5 Conclusion	53
Chapter 4 . Real-time 3D visualization method based on dual-dimensional imaging	54
4.1 Introduction.....	54
4.2 Dual-dimensional imaging.....	57
4.2.1 2D/3D simultaneous imaging.....	57

4.2.2 Light field upsampling in dual-dimensional imaging	62
4.2.3 Real-time light field upsampling using parallel computation	67
4.2.4 Experimental results.....	69
4.3 Real-time 3D visualization method based on dual-dimensional imaging	74
4.3.1 Light field display for dual-dimensional imaging.....	74
4.3.2 Real-time layer image generation using parallel computation	79
4.3.3 Simulation results.....	82
4.3.4 System implementation and experimental results.....	85
4.4 Conclusion	88
Chapter 5 . Conclusion.....	89
Bibliography	93
Appendix 103	
초 록 104	

List of Tables

Table 2.1 Calculated f-numbers of the elastic micro lens array from the measured profile.	19
Table 3.1 Specifications of real-time 3D visualization system based on light field imaging and integral imaging system.	37
Table 3.2 Specifications of the implemented real-time integral imaging system for light field microscopy.	49
Table 4.1 Specifications of the light field upsampling simulation in dual-dimensional imaging system.	63
Table 4.2 Specifications of the implemented dual-dimensional imaging system.	73
Table 4.3 Specifications of the implemented light field display system.	85

List of Figures

Figure 1.1 Schematic diagrams for light field imaging systems: (a) a lens array pickup type, and (b) a light field camera type.	2
Figure 1.2 Schematic diagrams for light field imaging system. The lens position indicates the lateral component of the light field (u, v) and the relative position of the pixel behind the lens represents the directional information (s, t).....	4
Figure 1.3 Example of view image separations in a parallax barrier multi-view display. The observer can watch the separated view images at the observing plane.	6
Figure 1.4 Principle of integral imaging system. The observer can watch the reconstructed 3D images at any position within a certain viewing angle.	7
Figure 2.1 The f-number matching problem in light field microscopy: (a) schematic diagram of the light field microscopy when the f-number of the micro lens array is (b) lower or (c) higher than the image-side f-number of the objective, and (d) when the f-number matching condition is satisfied.	12
Figure 2.2 Fabrication process of a PDMS micro lens array with the micro contact printing method. This method could replicate various types of micro lens arrays in a room temperature condition.....	15
Figure 2.3 The light field microscope setup with a 2D stretching device: (a) the customized 2D stretching device with an elastic micro lens array and (b) the light field microscope setup with the elastic micro lens array.	16
Figure 2.4 The surface profile of the PDMS lens array with the different strain levels measured by a 3D profiler. The surface height z is measured along the x direction in $0.625 \mu\text{m}$ intervals. R denotes the number	

	of rotations of the marker, and the higher R indicates the higher strain level.	18
Figure 2.5	Captured light field images of the light field microscope system using three types of the objective lenses ($4\times/0.13\text{NA}$, $20\times/0.5\text{NA}$, and $40\times/0.65\text{NA}$) with the different strain levels ($R = 0, 1$, and 2).21	
Figure 2.6	Reconstructed perspective view images of a piece of aloe captured with the light field microscope system with a $20\times/0.5\text{NA}$ objective lens and different strain levels: (a) $R = 0$ ($76 \times 66 \times 10 \times 10$), (b) $R = 1$ ($75 \times 64 \times 11 \times 11$), and (c) $R = 2$ ($74 \times 62 \times 12 \times 12$).	23
Figure 3.1	The schematic diagram of (a) multiple camera pickup method and (b) multi-view display.	28
Figure 3.2	The schematic diagram of (a) lens array pickup method and integral imaging display system (b) without the real-time elemental image generation algorithm and (c) with the real-time elemental image generation algorithm.....	29
Figure 3.3	The example of real-time elemental image generation algorithm: (a) captured image and (b) generated elemental image with $k = 0$, (c) $k = 1$, and (d) $k = 2$	32
Figure 3.4	The schematic diagram of the real-time 3D visualization system based on lens array pickup, real-time elemental image generation, and the integral imaging system.....	33
Figure 3.5	Principles of gap control method with depth plane adjustment method: (a) color separation problem in integral imaging, (b) gap control method, (c) gap control method with depth plane adjustment, (d) simulation result of color separation ($g = f$), (e) gap control method ($k = 0, g = 1.5f$), and (f) gap control method with depth plane adjustment ($k = 1, g = 1.5f$).	35
Figure 3.6	The implemented real-time 3D visualization system based on lens array pickup and integral imaging.....	39

Figure 3.7	Experimental results of real-time 3D visualization system: (a) left view, center view, and right view of reconstructed 3D images, (b) real-time 3D visualization of objects, and (c) reconstructed 3D image of 3D objects and a human hand.	40
Figure 3.8	Experimental results of proposed real-time capturing and 3D visualization system with different k values: (a) when central depth plane is located around hamburger object ($k = 1$) and (b) when central depth plane is located 1 cm behind mushroom object ($k = 2$).	41
Figure 3.9	The schematic diagram of the real-time integral imaging system for light field microscopy: (a) light field capturing with a light field microscope and (b) 3D image reconstruction using an integral imaging system.....	43
Figure 3.10	part of captured light field of <i>c.elegans</i> with a light field microscope with 40×/0.65 NA objective, Fresnel Tech. 125 μm micro lens array (focal length 2.5 mm): (red) 2 by 2 micro lens array region, (yellow) objective aperture stop, (sky blue) region that can be expressed with display lens array (1 mm lens array with 3.3 mm focal length).	46
Figure 3.11	The elemental image generation from a captured light field with f-number matching: (a) a part of the captured light field with LFM, (b) rearranged image by cropping image regions that can be expressed with the display lens array, and (c) generated elemental image using the pixel mapping algorithm ($k = 0$).	47
Figure 3.12	The implemented real-time integral imaging system for light field microscopy.	48
Figure 3.13	Experimental results for the implemented light field microscope: (a) the captured light field image of <i>c.elegans</i> , (b) perspective views extracted from captured light field image.	50

Figure 3.14	Experimental results for the proposed real-time integral imaging system for light field microscopy: (a) perspective views of reconstructed 3D images and (b) the conceptual video of real-time 3D experiment.....	51
Figure 4.1	The schematic diagram of the real-time 3D visualization system based on dual-dimensional imaging and a light field display.....	55
Figure 4.2	The example of the light field imaging of the two points: (a) The schematic diagram of the light field imaging system and (b) The captured light field image.....	57
Figure 4.3	The principle of the light field analysis and generation of the depth slice image: (a) The light field imaging system of the two plane objects and (b) The captured light field in spatio-angular domain and the depth slice image generated with the light field projection.....	58
Figure 4.4	The principle of the Fourier slice photography theorem : The light fields that are started from a certain depth form a line with the slope z in spectral domain.	59
Figure 4.5	The schematic diagram of the dual-dimensional imaging system.	61
Figure 4.6	The principle of light field upsampling in dual-dimensional imaging system: (a) Original light field, (b) Original light field spectrum, (c) Captured 2D image, (d) 2D Fourier transform of captured 2D image, (e) Captured light field, (f) 4D Fourier transform of captured light field, and (g) Spectrum of upsampled light field. Note that the line $f_\theta = 0$ in the light field spectrum domain is substituted to (d).	62
Figure 4.7	The simulation results of dual-dimensional imaging system: (a) captured 2D image and (b) captured light field image.....	64
Figure 4.8	The simulation results reconstructed perspective view images of (left) original light field, (center) light field from light field imaging, and (right) light field from dual-dimensional imaging...	66

Figure 4.9 The pipeline of the real-time light field upsampling using parallel computation.....	67
Figure 4.10 The calculation time of light field upsampling for various image size. Each value is the average of 100 calculations.....	69
Figure 4.11 The implemented dual-dimensional imaging system.....	70
Figure 4.12 The captured images with dual-dimensional imaging system: (a) captured light field image, (b) captured 2D image, (c) light field image after calibration, and (d) 2D image after calibration.	71
Figure 4.13 The reconstructed view images using (left) light field imaging only and (right) dual dimensional imaging.	72
Figure 4.14 The reconstructed view videos using dual dimensional imaging.	73
Figure 4.15 The light field display based on two stacked IPS-LCDs.....	75
Figure 4.16 The layer image optimization method for light field display: (a) the schematic diagram of the light field display and (b) non-linear least squares problem of stacked light field display.	77
Figure 4.17 The example of the optimized layer images for the light field display.	78
Figure 4.18 The pipeline of the real-time layer image optimization for light field display with parallel computing.....	79
Figure 4.19 The calculation time for the light field upsampling and the layer image optimization for various image size. Each value is the average of 100 calculations.	81
Figure 4.20 The simulation result of real-time layer image optimization: (a) reconstructed perspective view images of (left) original light field, (center-left) light field from light field imaging, (center-right) light field from dual-dimensional imaging and (right) reconstructed light field via light field display and (b) optimized layer images..	83
Figure 4.21 The simulation result of real-time layer image optimization with captured light field images from dual-dimensional imaging system:	

(a) reconstructed perspective view images of (left) light field from light field imaging, (center) light field from dual-dimensional imaging and (right) reconstructed light field via light field display and (b) optimized layer images. 84

Figure 4.22 The implemented light field display system for dual-dimensional imaging system..... 86

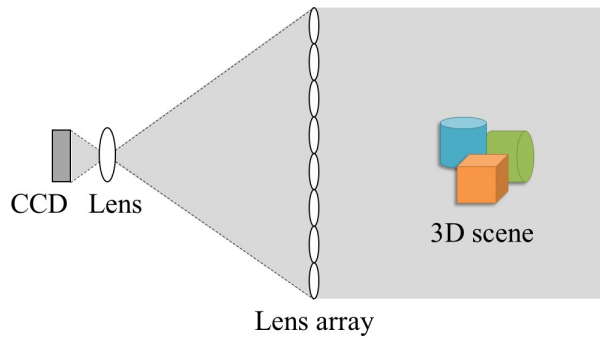
Figure 4.23 The experimental results of 3D visualization of c.elegans with light field display: reconstructed perspective view images of (left) upsampled light field from dual-dimensional imaging, (center) reconstruction simulation of light field display and (right) experimental results with implemented light field display system.87

Chapter 1 . Introduction

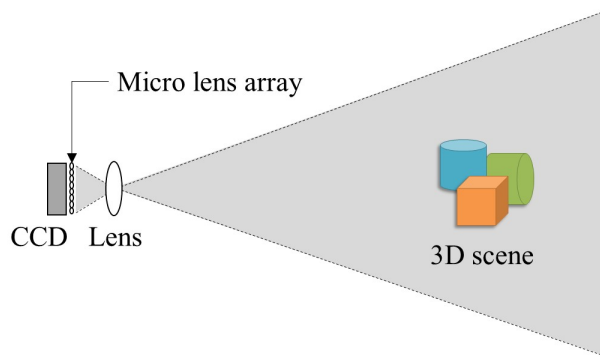
All human beings like to record their valuable moments and preserve them for a long time. Even thirty thousand years ago, ancient humans drew paintings of horses and mammoths at Chauvet cave [1]. With advances in technology, this desire of documentation has been expressed as paintings, voice recordings, photographs, and videos. Nowadays, people can make their own videos with their smart phones, play them any time, and keep them permanently. However, they are still excited to capture 360-degree scene with virtual reality (VR) cameras [2]. Since this world is three-dimensional (3D) and people perceive information every time from this world, they wish to record and reconstruct this world as the way they recognize this world, in 3D.

In this point of view, recording 3D scene and its reconstruction have an important meaning to human happiness as well as industrial technology. Companies have commercialized a number of 3D imaging devices with various technologies [4–10]. Time-of-Flight (ToF) camera is one of them, which can resolve the distance using the speed of light [4]. ToF camera measures the time that light travels from the camera to each point in 3D scene. By the way, structured light calculates the depth information from the captured image of the reflection of coded light patterns [5]. Both technologies are utilized in gaming, computer vision, topography and self-driving cars because they can obtain the depth map directly from the scene in real-time with a high resolution. However, the obtained depth map

information should be converted to perspective view images before delivered to observer, which costs additional computational time.



(a)



(b)

Figure 1.1 Schematic diagrams for light field imaging systems: (a) a lens array pickup type, and (b) a light field camera type.

Multiple cameras can capture and provide perspective view images immediately [6]. For example, a stereo camera consists of horizontally connected two image sensors like human vision system. However, the multiple camera system needs to be in alignment, and they cannot provide

depth information directly. Larger number of cameras requires more space and higher complexity in alignment.

Light field imaging method, which captures 3D scenes with a lens array, works as two-dimensional (2D) camera array system with the reduced resolution [8–21]. Figure 1.1 shows two major types of light field imaging systems. One is to locate a lens array in front of the 3D scene and set the camera focus at the back focal plane of the lens array as shown in Fig. 1.1(a). The other method is to locate a micro lens array in front of a charge coupled device (CCD) and an imaging lens images the 3D scene at the micro lens array plane as shown in Fig. 1.1(b). In latter, the distance between the micro lens array and CCD should be equal to the focal length of the micro lens array. Both configures can capture the light field image of the 3D scene, which contains directional information.

Light field is an idea based on geometrical optics to approximate light as a straight ray carrying the color information [11, 12, 22]. A light ray l can be expressed as a point of contact (u, v) between the light ray and the reference plane and the direction vector (s, t) . As shown in Fig. 1.2, a light field imaging system can record the lateral positions of the light rays and their directions at the lens array plane. In detail, the lens position indicates the lateral component of the light field (u, v) and the relative position of the pixel behind the lens represents the directional information (s, t) . A light field imaging system can achieve the perspective view images in a single shot, but their resolutions are low. In addition, the light field imaging system has a compact structure compared to the multiple camera system, but the captured perspective views have lower parallax difference.

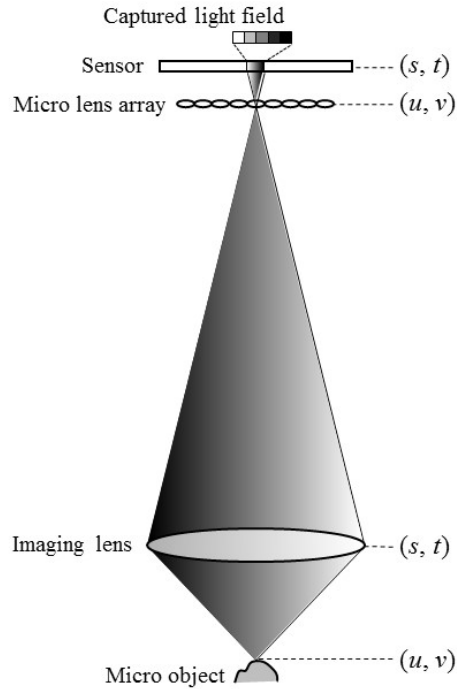


Figure 1.2 Schematic diagrams for light field imaging system. The lens position indicates the lateral component of the light field (u, v) and the relative position of the pixel behind the lens represents the directional information (s, t) .

3D information, obtained by various 3D imaging devices above, can be delivered to human through 3D display systems [18–21]. To provide a vivid and realistic 3D experience to observers, 3D display should be built on the understandings of human visual systems and how a person can perceive the depth information from nature [3, 19]. A man perceives 3D scene with physiological and psychological depth cues [23]. The former includes binocular disparity, accommodation, convergence, and motion parallax,

while the latter includes overlapping, gradient, shadow, and linear perspectives. Among them, the binocular disparity takes major roles for the perception of objects closer than 10 m [24]. Thus, most of the early 3D displays provided binocular disparity only [18].

Since Wheatstone introduced a system providing left-eye and right-eye views to viewers using mirrors, 3D display has been focused on the methods to separate the left-eye and right-eye view images [18]. The most of the methods have been based on the special aids in front of each eye. Anaglyph is to locate different color filters (red and cyan) in front of the left and right eyes for the separation of view images [25]. Shutter glass method utilizes shutter glasses synchronized with the display panel and distinguishes left and right eye images with time-multiplexing. Polarization glasses method uses a film-type patterned retarder, which has orthogonal polarizations (left-handed and right-handed) line by line and is attached to the display panel. By locating orthogonal polarization filter in front of left and right eye, the display system can provide binocular disparity to the observer with spatial multiplexing. These glasses-type 3D display systems accompany inconvenient experience caused by special aids in front of eyes [18]. Since these systems provide binocular disparity only, the other physiological depth cues compete with binocular disparity which may cause motion sickness [26–29].

Hence, the multi-view display system was introduced to provide 3D experiences to an observer at a certain position without glasses [30–34]. It spatially divides view images by controlling the directions of light rays using a parallax barrier or a lenticular in front of the display panel. Figure 1.3

shows an experimental result of the view separation with a parallax barrier and a display panel. By carefully designing the pitch and the thickness of the parallax barrier, one can distinguish the view images at the certain depth plane, and can deliver different view images to observer's left and right eyes. The multi-view display is free from glasses and can provide motion parallax as well as binocular disparity. However, the viewing distance is fixed and unchanged.

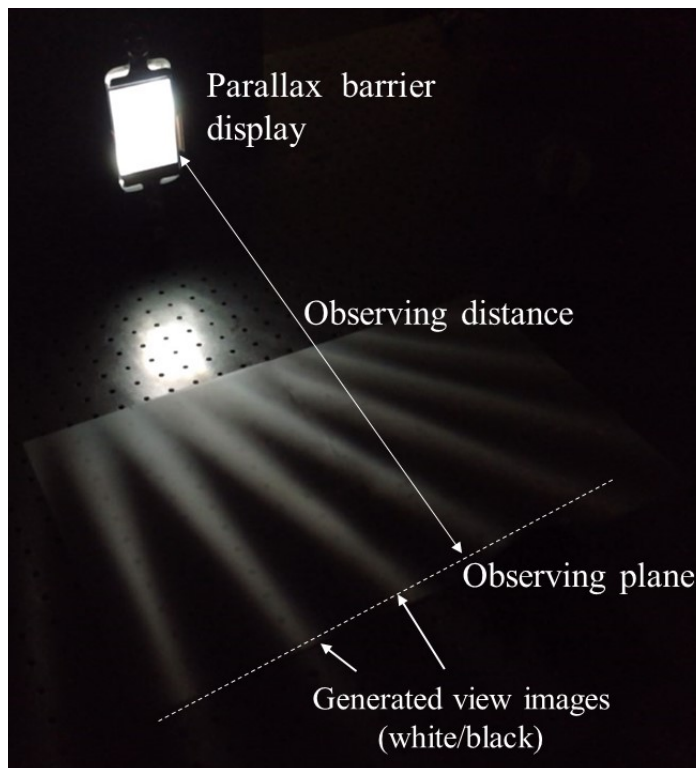


Figure 1.3 Example of view image separations in a parallax barrier multi-view display. The observer can watch the separated view images at the observing plane.

In contrast, integral imaging focuses on not the viewer's position but the optical reconstruction of light rays [35–38]. Figure 1.4 shows the principle of integral imaging. By using a 2D lens array in front of the display panel, one can generate the dense distribution of light rays at 3D space and reconstruct 3D images there. Integral imaging has a limitation on expressible depth range but no restriction on viewing distance. Furthermore, integral imaging provides continuous view images within a certain viewing angle but the resolution of the individual images is very low compared to multi-view display. In addition, integral imaging distributes the light rays uniformly regardless of displayed contents, which can cause inefficient usage of light rays. The required number of the light fields of target 3D scene may differ depending on the position, but the fixed lens array cannot change the distribution adaptively.

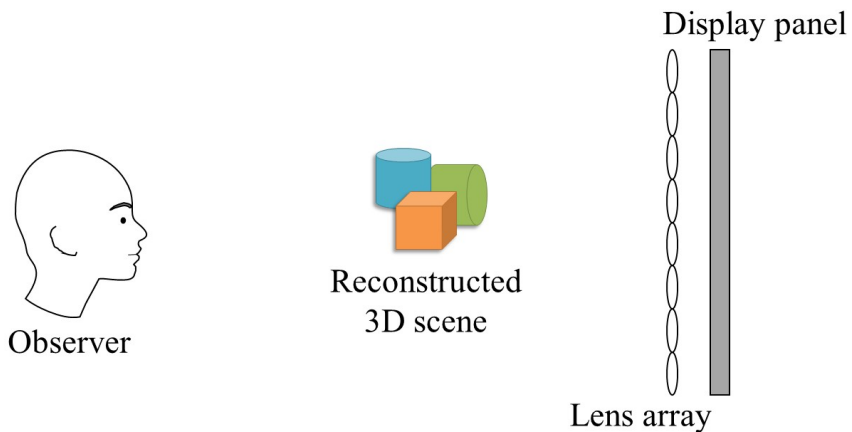


Figure 1.4 Principle of integral imaging system. The observer can watch the reconstructed 3D images at any position within a certain viewing angle.

Computational light field display was designed to enhance the resolution of 3D images by using the correlation between perspective view images [40–44]. Since the panel-type 3D display systems attempt to visualize 3D information with several 2D panels, it always suffers from the lack of data capacity. Therefore, the computational light field display calculates the optimized light field distribution for a given scene. This optimization problem is one type of non-linear least square problems, and can be solved with the iterative algorithm. The computational light field display is usually implemented by stacking the display panels and can achieve higher resolution compared to integral imaging. However, it requires pre-computational process for each frame which takes a long time. Recently, a real-time solver for the computational light field display was introduced based on parallel computation with a graphics processing unit (GPU) [44].

As above, 3D imaging and 3D display have been widely studied in separate ways. 3D imaging researchers have focused on the higher depth resolution and robust imaging systems while the researchers in 3D display have concentrated on the improvement of viewing characteristics. The real-time conversion of the obtained 3D information to the base image for 3D displays has not been studied deeply yet. However, capturing 3D information and visualizing it in 3D and in real-time has a significant meaning because the reason of 3D imaging is to provide the information to people. Therefore, the whole procedure of capturing, converting, and displaying 3D images should be carefully controlled. And this technology enables glasses-free 3D broadcasting and can be widely used in biomedical application [45–47].

Previously, several real-time glasses-free 3D display systems have been

presented. Multiple camera can provide the base image for the multi-view display with the interweaving process in real-time, but the system requires enough space for the cameras [7]. Integral imaging included capturing and displaying process together from the first, however it has suffered from depth reversion problem, which is often called pseudoscopic problem [48–51].

The real-time 3D visualization method can be effectively realized with a light field imaging system, a light field display system, and a real-time light field processing algorithm. Among the various 3D imaging technologies, the light field imaging can obtain the 3D information from micro-scale to real-scale objects with one-shot without any additional device except a lens array. The 3D deconvolution [11–13] and virtual 3D reconstruction [9, 18, 36–38] in light field imaging have been introduced from several groups, however, the optical 3D reconstruction and the real-time optical 3D reconstruction have not been referred.

In this dissertation, I propose a real-time 3D visualization method based on light field imaging and light field display. 3D information is obtained with light field imaging and light field microscope systems and converted to elemental images for the integral imaging system or layer images for computational light field display systems. The effective f-number matching method using an elastic micro lens array is also presented to enhance the resolution in light field imaging. In Chapter 2, an f-number matching problem and a new f-number matching method are introduced with an elastic micro lens array in light field imaging. In Chapter 3, a real-time 3D visualization method is introduced based on light field imaging and integral imaging. In Chapter 4, dual-dimensional imaging method is proposed to

achieve the high resolution light field images. A dual-dimensional imaging system captures a light field image and a 2D image simultaneously with a half mirror and two synchronized CCDs, as this additional 2D image can enhance the resolution of the light field images. This upsampled light field images are provided to the observers with a light field display in real-time. This dissertation ends with the conclusion in Chapter 5.

Chapter 2 . F-number matching method using elastic micro lens array in light field microscopy

2.1 Introduction

Light field microscopy obtains 3D information of a micro object in one shot by using a large NA objective lens and a micro lens array located at the image plane of an optical microscope [10–15]. As shown in Fig. 2.1(a), the micro lens array at the image plane enables the recording of a 4D light field with a CCD. The optical property of the micro lens array determines the ratio of the lateral and angular resolution of the obtained light field. However, not every micro lens array can be used in the light field microscope system. The f-number of the micro lens array should be matched with the image-side f-number of the objective lens [10–13].

In this chapter, a new f-number matching method is introduced for various types of an objective lens by using an elastic micro lens array. An elastic micro lens array is fabricated with polydimethylsiloxane (PDMS) and analyzed its strain characteristics. The f-number variance of the fabricated elastic micro lens array is measured with a 3D profiler and the idea is verified with a light field microscope experiment.

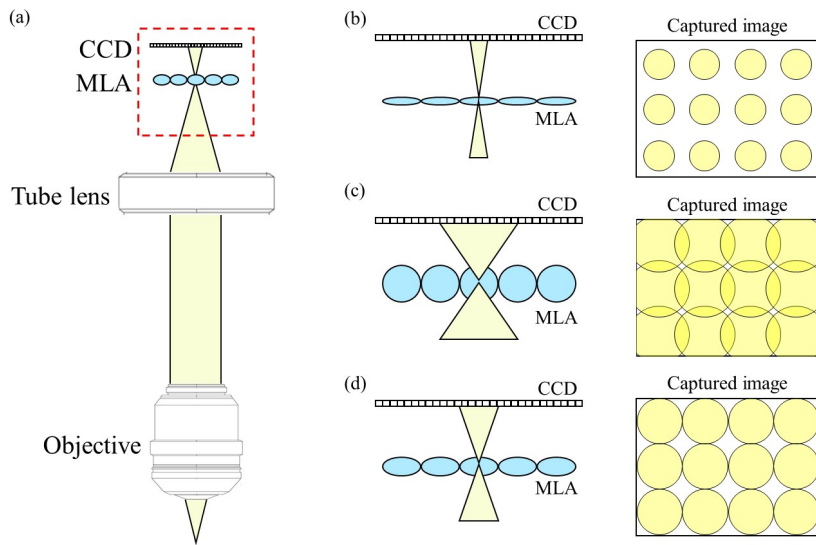


Figure 2.1 The f-number matching problem in light field microscopy: (a) schematic diagram of the light field microscopy when the f-number of the micro lens array is (b) lower or (c) higher than the image-side f-number of the objective, and (d) when the f-number matching condition is satisfied.

2.2 F-number variation of elastic micro lens array

2.2.1 F-number matching problem in light field imaging

Figures 2.1(b)-2.1(d) show the f-number matching issue in light field microscope. If the f-number of the objective lens is higher or lower than that of the micro lens array, the diameter of the captured light field circles is smaller or larger than the micro lens array pitch, respectively. To utilize all the resolution of the CCD, two f-numbers should be equal, as shown in Fig. 2.1(d). The precise f-number matching is crucial to the imaging quality because the light field microscope sacrifices 2D resolution to obtain a 4D light field. The f-number matching equation is derived as follows:

$$F = \frac{f}{D} = \frac{M}{2NA}, \quad (2.1)$$

where F is the f-number of the micro lens array, f and D are the focal length and the lens pitch of the micro lens, respectively, and M and NA are the magnitude and the NA of the objective lens, respectively. Since the image-side f-number of an objective lens is proportional to its magnitude, one type of the micro lens array can be applied to several objective lenses with different magnitudes [10, 46, 52]. However, each objective lens generally requires a paired micro lens array with the specific f-number, which requires a complex system and is expensive.

2.2.2 Fabrication of elastic micro lens array with PDMS

To be applied to the multiple objective lenses in the light field microscope systems, an elastic micro lens array was fabricated with PDMS. There have been several previous studies on the fabrication of elastic micro lens arrays based on photolithography [53–57]. However, these fabrication methods are expensive, time consuming, and can be applied to limited specifications of micro lens arrays only. Here, a micro contact printing method is applied to fabricate elastic micro lens array replicas from commercial micro lens arrays [58, 59]. As a base material, PDMS, which has been widely used for elastic micro lens array fabrication [56–60], is applied.

Figure 2.2 shows the fabrication process of an elastic PDMS micro lens array. At first, the 10:1 mixture of PDMS elastomer (Dow Corning Sylgard-184) and cross-linking agent (Dow Corning) was poured onto commercial micro lens arrays. a fused-silica micro lens array was used as the original mold (125 μm lens pitch / 1.66 mm focal length). The mixture was cured at 100°C for 1 h. After curing, the concave PDMS micro lens array mold was detached from the mold and immersed in a surfactant solution for 15 min. After immersion, the concave mold is rinsed in distilled water. Next, another PDMS mixture is poured and cured onto the mold. After curing the mold at 100°C for 1 h and detaching it, an elastic PDMS micro lens array can be obtained. In the fabrication, the micro lens array and the substrate parts are set to have a similar thickness for the complete 2D stretch; otherwise, the micro lens array plane could be bent.

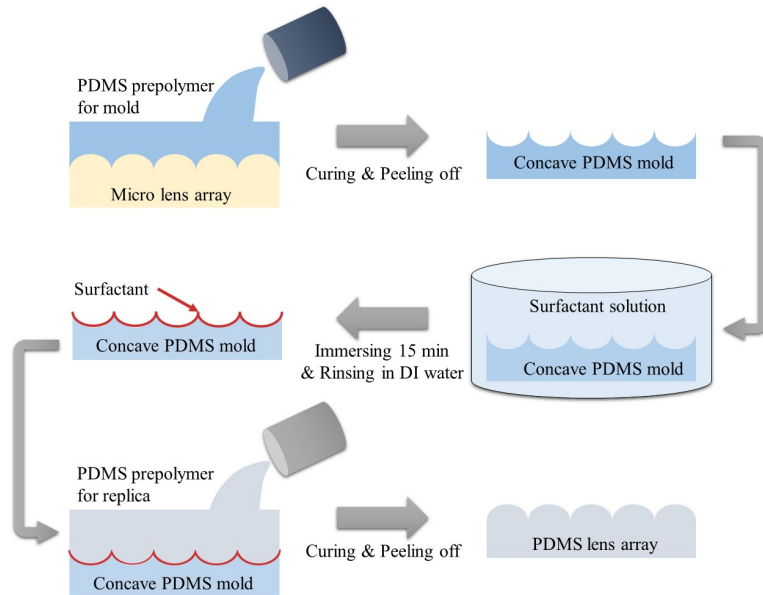


Figure 2.2 Fabrication process of a PDMS micro lens array with the micro contact printing method. This method could replicate various types of micro lens arrays in a room temperature condition.

In the fabrication process, a different material called ultraviolet-curable monomer (NOA, Norland NOA86) was also tried to overcome the weak points of the PDMS micro lens array. Detaching the PDMS micro lens array from the concave PDMS mold can damage the surface profile because PDMS-PDMS interaction is strong. Since NOA-PDMS interaction is weaker, however, more clear and robust micro lens arrays were obtained. Nevertheless, PDMS micro lens arrays was adopted because NOA had worse transparency and elasticity. NOA became a little bit yellowish after curing, and NOA micro lens arrays remained stretched after the strain response test. Therefore, PDMS would be the better option for the fabrication.

2.2.3 Strain response and F-number variation

Figure 2.3(a) shows one example of the fabricated elastic micro lens array and the customized 2D stretching device. To address same strain to each micro lens, the total size was set to be much bigger than the original micro lens array's size. In the system, the total size is around $40\text{ mm} \times 40\text{ mm}$ while the micro lens array part is $10\text{ mm} \times 10\text{ mm}$ at the center. To stretch the PDMS micro lens array uniformly, the micro lens array part was located at the center of PDMS substrate and the stretch clamps at the four edges of the substrate, as shown in Fig. 2.3(a).

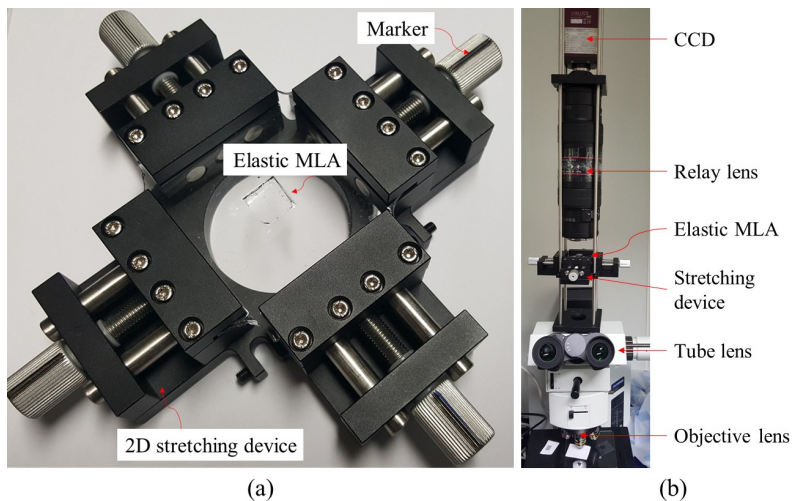


Figure 2.3 The light field microscope setup with a 2D stretching device: (a) the customized 2D stretching device with an elastic micro lens array and (b) the light field microscope setup with the elastic micro lens array.

The total volume of the PDMS is known to be preserved in the different strain levels (Poisson ratio of ~ 0.5). Chandra *et al.* introduced a strain

response analysis of the PDMS micro lens array based on the volume conservation equation [57]. However, in this case, the substrate is stretched as well as the micro lens array, and the total thickness can be changed with the strain. Therefore, the structure of the micro lens array was directly measured in different strain levels with a 3D profiler (NanoFocus, μ Surf).

Figure 2.4 shows the measured profile of the micro lens array with the different strain levels. R denotes the number of rotations of the marker, which corresponds to the distance change of the stretching device. A one-level difference in R indicates 2.4 mm change in both directions. Note that the stretching distance of the stretching device was different from the actual stretched length of the micro lens array part, but the higher R indicates the higher strain level. The 3D profiler measured the surface in 0.625 μm intervals. Note that the nodes in Fig. 2.4 do not indicate all the measured points but a few of them. There are nine more measurements between the nearby nodes.

Based on Eq. (2.1), f-number variation of the fabricated micro lens array can be calculated. Table 2.1 shows the calculated f-numbers from the measured profile in Fig. 2.4. The measured profiles showed that the fabricated elastic micro lens array has spherical shapes as the original micro lens array does. The focal lengths were calculated from the surface profile by a ray optics simulation. The fabricated elastic micro lens array without strain ($R = 0$) has 125.00 μm lens pitch and 1898.2 μm focal length. Compared to the specification of original mold (125 μm pitch/1660 $\mu\text{m} \pm 5\%$ focal length), the surface profile of the replica accords well with the original mold, but the refractive index is different (1.50 for original mold/1.38 for PDMS). As the

strain level increases, the f-number of the micro lens array gradually increases as well from 15.19 to 19.33 (27.3%). Since the stretching device used in the experiment did not hold the four corners as shown in Fig. 2.3(a), the micro lens array began to tear into two parts from the corners with the large strain levels. The average stretching limit of the micro lens arrays was around $R = 5$, but this limitation could be improved easily by changing the stretching device.

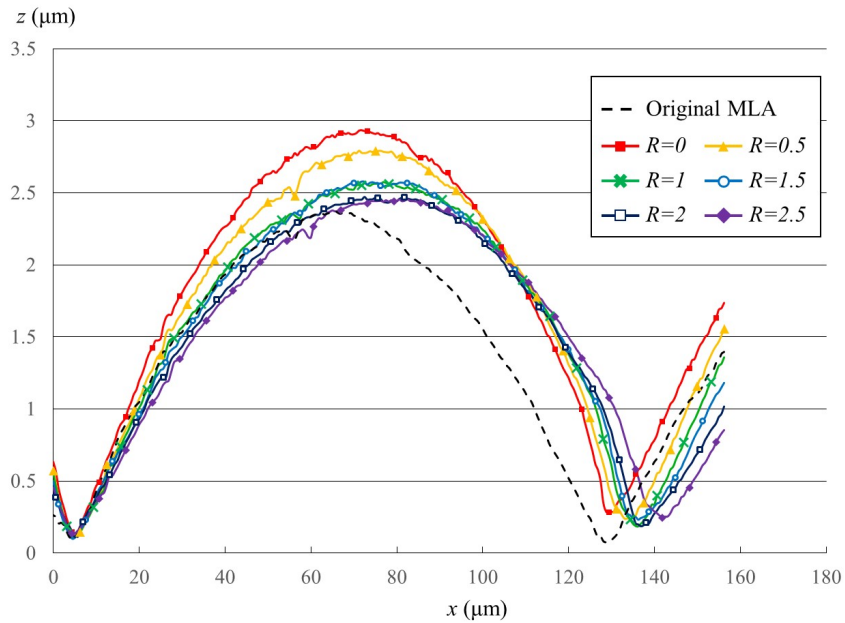


Figure 2.4 The surface profile of the PDMS lens array with the different strain levels measured by a 3D profiler. The surface height z is measured along the x direction in $0.625 \mu\text{m}$ intervals. R denotes the number of rotations of the marker, and the higher R indicates the higher strain level.

Table 2.1 Calculated f-numbers of the elastic micro lens array from the measured profile.

Strain	D (μm)	f (μm)	F
Original MLA	125.31	1660.0	13.25
$R = 0$	125.00	1898.2	15.19
$R = 0.5$	130.63	2059.2	15.76
$R = 1$	132.19	2335.3	17.67
$R = 1.5$	132.19	2366.0	17.90
$R = 2$	134.06	2543.1	18.97
$R = 2.5$	137.81	2663.5	19.33

The relation between the strain level and the f-number is also interesting. The focal length f and the lens pitch D both increase as the strain level increases; however, the f-number F ($= f / D$) increases gradually, too. a clue could be found from the previous study on the strain response of a PDMS micro lens array [57] that the focal length variation correlates to the complex polynomial of D , and f increases more rapidly than D . In the experiment, as mentioned above, the previous study cannot be applied directly due to substrate volume, but its tendency is still valid and explains the f-number variation clearly.

2.3 F-number matching method using elastic micro lens array

A light field microscope setup was built with the fabricated elastic micro lens array and the stretching device. Figure 2.3(b) shows the implemented light field microscope setup. A transmission-type optical microscope (Olympus BX-51T), two camera lenses (Canon EF 100 mm f/2.8 Macro USM), a CCD (AVT Prosilica GX2300C), and the 2D stretching device with the elastic micro lens array were used. Note that the lenses were connected nose-to-nose. An optical jig was mounted on the tube lens for the components' calibration. For the experiment, three objective lenses with different f-numbers were used: 4×/0.13NA (f-number: 15.38), 20×/0.5NA (f-number: 20), and 40×/0.65NA (f-number: 30.77). The identical elastic micro lens array employed in the surface profile test was used (f-number: 15.19–19.33). A piece of white paper was used as a specimen to observe clear and maximum light field circles.

Figure 2.5 shows the captured light field images of the light field microscope system using three types of the objective lenses with three different strain levels. Note that the cropped images show the same nine micro lenses at the central region of the micro lens array. The resultant image circles with the 4× objective are bigger than those of the 20× objective at the same strain level because the f-number of the 20× objective is larger than that of the 4× objective. The average ratio of the measured diameters of the light field circles between two objectives is 1.29, which almost agrees with

the 1.30 ratio of the f-number of the objectives. This accordance implies that the setup satisfies two basic conditions of the light field microscope: the micro lens array is located at the image plane of the optical microscope, and the CCD focuses on the back focal plane of the micro lens array.

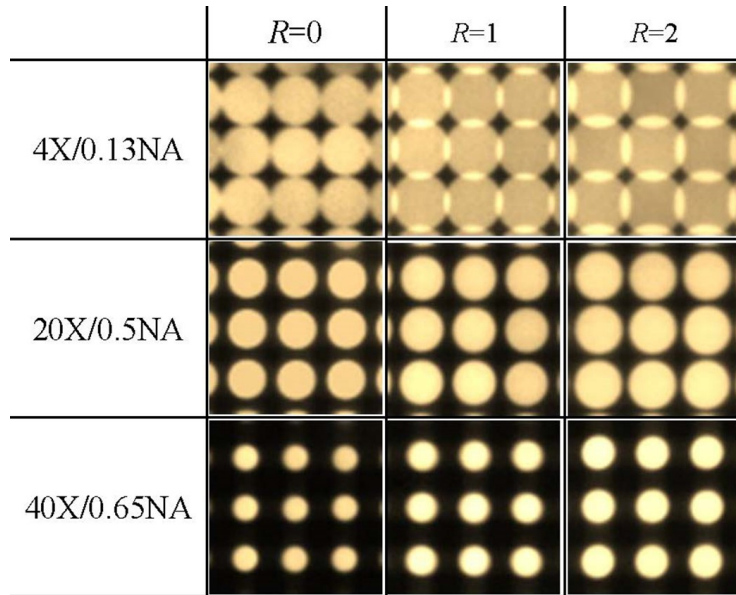


Figure 2.5 Captured light field images of the light field microscope system using three types of the objective lenses (4×/0.13NA, 20×/0.5NA, and 40×/0.65NA) with the different strain levels ($R = 0, 1,$ and 2).

The diameter of the light field circles in the captured image increases as the strain level increases, where it is directly proportional to the f-number of the micro lens array. Therefore, this result is in agreement with the f-number variation experiment result shown in Table 2.1. The results verify that the presented light field microscope system with the elastic micro lens array can

change its f-number and can be applied to the multiple objective lenses. For the 4×/0.13NA objective lens, the strain level could be chosen around $R = 0$, and, for the 20×/0.5NA objective lens, the higher ($R > 2$) strain level would be chosen. One nice part of this f-number matching method is that the observer does not have to calculate the f-number and the strain level. The observer can just change the strain level back and forth to make clear and full light field circles, which guarantees matched f-numbers.

Figure 2.6 shows the reconstructed perspective view images with a 20×/0.5NA objective lens and different strain levels. A piece of aloe was used as the specimen. As strain level increased, the light field circle got bigger, and a larger CCD region could be utilized, as shown in the second row of Fig. 2.5, and the resultant reconstructed image contained more information. When $R = 0$, 10×10 perspective view images were reconstructed, and their individual resolution was 76×66 . By contrast, when $R = 2$, 12×12 view images were reconstructed and their individual resolution was 74×62 . Note that their resolution slightly decreased because of stretched lens pitch. Since the view images contained the light field information with the same NA, angular resolution was improved, and more detailed angular information could be obtained of the 3D scene.

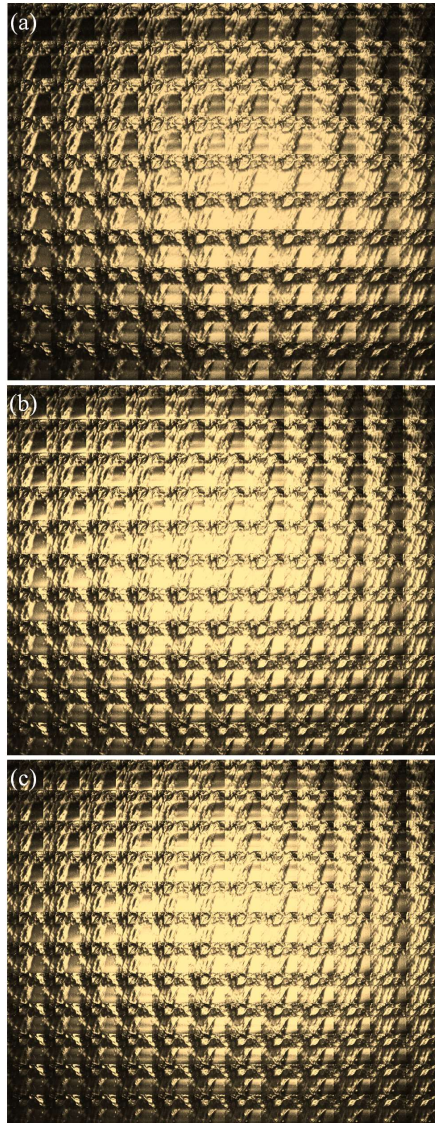


Figure 2.6 Reconstructed perspective view images of a piece of aloe captured with the light field microscope system with a $20\times/0.5\text{NA}$ objective lens and different strain levels: (a) $R = 0$ ($76 \times 66 \times 10 \times 10$), (b) $R = 1$ ($75 \times 64 \times 11 \times 11$), and (c) $R = 2$ ($74 \times 62 \times 12 \times 12$).

2.4 Conclusion

In this chapter, a new f-number matching method in light field microscopy was proposed with using an elastic PDMS micro lens array. The proposed elastic PDMS micro lens array fabrication method not only was fast and low cost but also could replicate various types of micro lens arrays in a room temperature condition with a precise estimation of the output lens pitch and focal length. The fabricated elastic micro lens array could change its f-number up to 27.3% with the 2D stretching device and could be applied to the multiple objective lenses in the light field microscope system. The results verified that the proposed method can reduce the form factor and the cost of the light field microscope system, and this work would help to give a deeper understanding of elastic micro lens array fabrication and its strain response.

The proposed method can be applied to not only the light field microscope but also the light field camera. The commercial light field camera using a zoom lens changes the focal length of the main lens, and the f-numbers are matched only at the minimum focal length. Therefore, the light field camera cannot utilize its resolution fully in most cases. The proposed method, however, could utilize the whole CCD with an elastic micro lens array and a stretching device coupled with the zoom lens, which can dramatically improve the image quality of the zoomed scene. Since the fabrication process is based on the soft-lithography, the hexagonal elastic micro lens array can be easily obtained with the similar process, which is widely used in the light field camera because of its higher fill factor.

Chapter 3 . Real-time 3D visualization method based on light field imaging

3.1 Introduction

Visualizing a real object in three-dimensional (3D) space has been one of the main issues in 3D industries [6–9, 48–51]. It is possible to extract 3D information from objects using a multicamera [6], a time of flight camera [4], a structured light method [5], or a lens array [9, 10]. Among them, only a few methods are actually functional in real-time with 3D display systems such as stereoscopy, multi-view or integral imaging, which is a key technology for 3D broadcasting [6, 7, 48–51]. Since stereoscopy and multi-view systems provide several view images, their base image can be easily generated by means of a multi-camera method [6, 7]. However, the multi-camera capturing method requires a large space, a delicate alignment between cameras, and a relatively high computational load for post processing.

For an integral imaging system, a set of elemental images can be obtained with a camera and a lens array as introduced by Lippmann in 1908 [35]. The lens array capturing method is less bulky and is not constrained by alignment problems [36–38]. However, if the captured image is used as the set of elemental images without post-processing, the reconstructed 3D image

is pseudoscopic [48–51]. In the past decades, several methods have been proposed for solving the pseudoscopic problem, but most cannot satisfy real-time conditions [50], cannot provide a real 3D image [8] or they have a need of special optical devices [51]. Until now, there have not been a real-time integral imaging system providing real images without pseudoscopic problem [61–72].

Multiple camera pickup method can be applied to real-time 3D visualization with multiview display without pseudoscopic problem [6]. However, it is bulky and needs careful calibration between multiple cameras. Lens array pickup method is simple and free from calibration between cameras, but it suffers from pseudoscopic problem. To realize real-time capturing and 3D visualization using benefits of lens array pickup method and integral imaging, our group focused on this inequality between two pickup methods. Why there is no pseudoscopic problem in multiple camera pickup method and multi-view display? Our group reached to a simple difference that there was not any interweaving process between lens array pickup method and integral imaging.

In this chapter, a real-time 3D visualization method is proposed based on light field imaging and integral imaging. In Chapter 3.2, a real-time elemental image generation algorithm is introduced which is free from pseudoscopic problem. Based on this pixel mapping algorithm, a real-time 3D visualization system is implemented for real-scale objects based on a lens array pickup method and an integral imaging display system in Chapter 3.3. In Chapter 3.4, this idea is expanded to micro-scale objects which can be realized with a light field microscope and an integral imaging display system.

The proposed systems can provide real-time real mode 3D images with an integral imaging display system for a real-scale and micro-scale objects.

3.2 Real-time elemental image generation algorithm

As mentioned above, real-time pixel mapping algorithm is inspired by interweaving process of multiple camera pickup and multi-view display. In multi-view interweaving process, all the pixels in multiple CCDs are back propagated to corresponding display pixels through lenticular lens. Therefore, multi-view display system provides several view images at specific viewpoints, which are the exact position of pickup CCDs. Figure 3.1 shows the schematic diagram of multiple camera pickup method and multi-view display. In multi-view display, viewing distance is fixed by the distance between pickup CCDs and convergence plane and there is no depth reversion problem. The interweaving algorithm generates the one base image from the images captured from the multiple cameras.

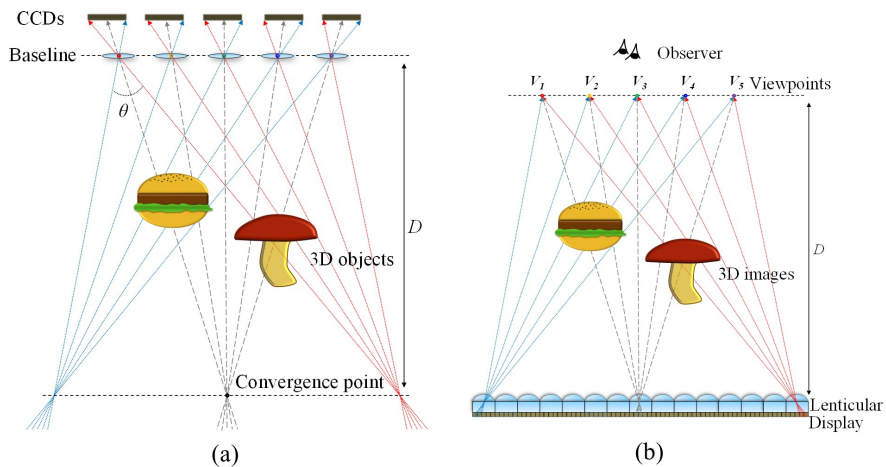


Figure 3.1 The schematic diagram of (a) multiple camera pickup method and (b) multi-view display.

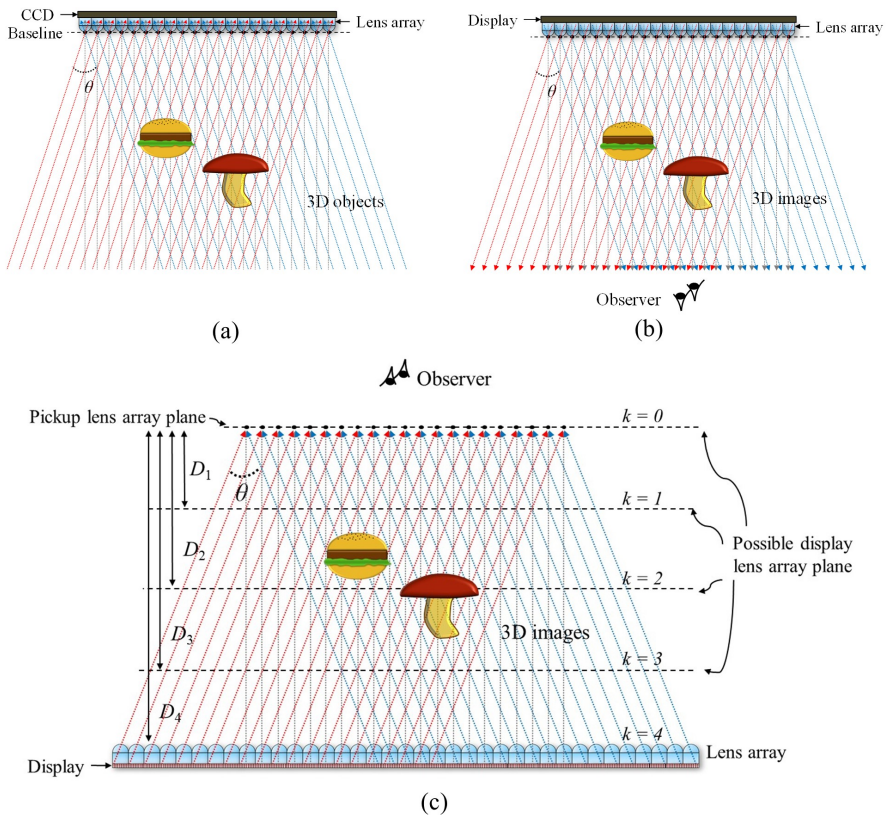


Figure 3.2 The schematic diagram of (a) lens array pickup method and integral imaging display system (b) without the real-time elemental image generation algorithm and (c) with the real-time elemental image generation algorithm.

Real-time elemental generation algorithm works with the same principle. The algorithm generates an elemental image from the capture image with the consideration of relative positions between the pickup lens array plane and display lens array plane. Once the pickup lens array plane and the display lens array plane was decided, then the light fields from the pixels of CCD are

back propagated to display panel plane. In integral imaging, there is no viewing distance and each lens in lens array contains light field information with same viewing angle and same direction. Therefore, the distance between the pickup lens array plane and the display lens array plane can be adjustable. In fact, the distance can be one of the several lengths derived by lens pitch and display panel pixel pitch because the viewpoints planes are repeated by the geometric relation of them.

Figure 3.2 shows the schematic diagram of lens array pickup method with and without real-time elemental image generation algorithm. Integral imaging has used captured image as the elemental image directly as shown in Figs. 3.2(a) and 3.2(b) because Lippmann first introduced integral imaging in that way in 1908 [35]. This method can provide 3D images in real-time but their depths were reversed. Figure 3.2(c) shows several possible display lens array planes in real-time elemental generation algorithm. Compared to Fig. 3.2(b), reconstructed 3D images have correct depth information. The scheme is more similar to the multi-view display with a lot of pickup cameras which are in parallel direction as shown in Fig. 3.1. The distance between pickup lens array plane and k -th display lens array plane D_k is derived as follows:

$$D_k = \frac{p_l}{p_p} kf = knf, \quad (3.1)$$

where p_l is lens pitch, f is focal length of lens, p_p is display panel pixel pitch, and n is the number of pixels in a lens. For each k -value, corresponding display panel pixel and CCD pixel are changed. The mapping process can be simply derived by ray tracing algorithm, and the relation matrix is as follows:

$$\begin{pmatrix} i' \\ j' \\ s' \\ t' \end{pmatrix} = \begin{pmatrix} 1 & 0 & -k & 0 \\ 0 & 1 & 0 & -k \\ 0 & 0 & -1 & 0 \\ 0 & 0 & 0 & -1 \end{pmatrix} \begin{pmatrix} i \\ j \\ s \\ t \end{pmatrix} + \begin{pmatrix} kn \\ kn \\ n+1 \\ n+1 \end{pmatrix}, \quad (3.2)$$

where s -th and t -th CCD pixel of i -th and j -th lens of pickup lens array is mapped to the s' -th and t' -th display panel pixel of i' -th and j' -th lens of display lens array, respectively. Figure 3.3 shows some examples of pixel mapping algorithm for several k values, where the color indicates lens number and the number inside color indicates pixel number.

Figure 3.3(a) shows captured light field of 3D objects, and the corrected elemental image is obtained by pixel mapping of captured light field. Since the number of pixels behind each lens is identical for all lenses in lens array, the pixels with same number contain same directional information of 3D objects. Therefore, although the pixels are shuffled complexly after the real-time pixel mapping algorithm, the pixel number behind each lens cannot be changed as shown in Fig. 3.3. By changing k -value, the relative position between display lens array and 3D objects can be varied. This algorithm works in real-time regardless of k -value, and the depth of 3D object can also be easily adjusted from real to virtual images in real-time.

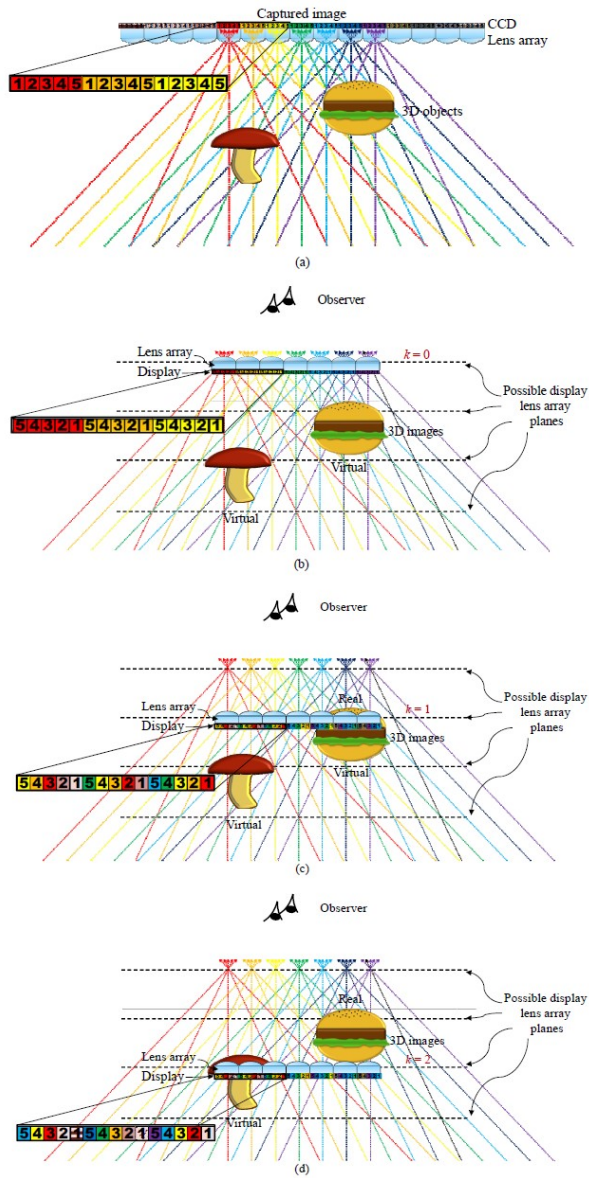


Figure 3.3 The example of real-time elemental image generation algorithm: (a) captured image and (b) generated elemental image with $k = 0$, (c) $k = 1$, and (d) $k = 2$.

3.3 Real-time capturing and 3D visualization method based on integral imaging

In this section, the real-time 3D visualization system is implemented based on the lens array pickup, real-time elemental image generation, and the integral imaging system. Figure 3.4 shows the schematic diagram of the implemented system. Before implementing, the quality of the reconstructed 3D images was analyzed as the display lens array plane varies with the k -value in the elemental image generation algorithm.

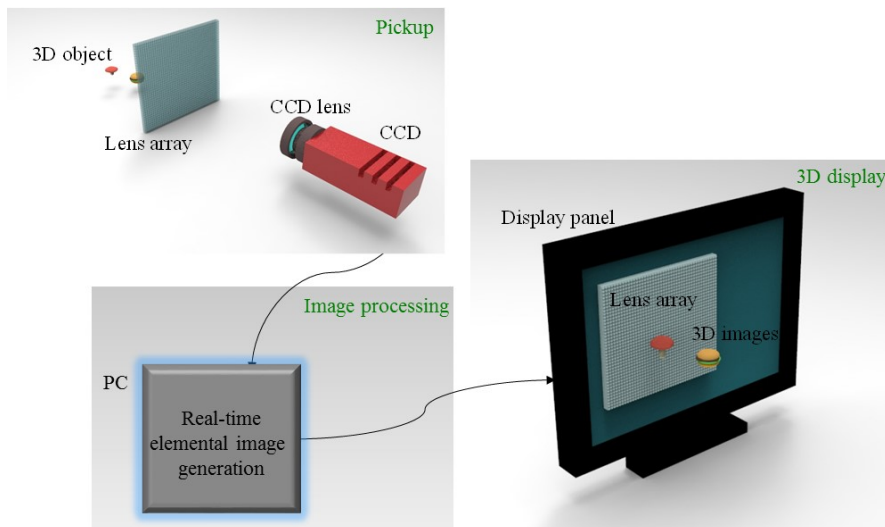


Figure 3.4 The schematic diagram of the real-time 3D visualization system based on lens array pickup, real-time elemental image generation, and the integral imaging system.

Adjusting depth plane not only locates 3D images from real to virtual images but also improves quality of reconstructed 3D images. In integral

imaging using liquid crystal display (LCD), color separation problem caused by red/green/blue (RGB) subpixels degrades image quality. Figure 3.5(a) shows color separation problem in integral imaging caused by RGB subpixels. Among several methods to improve image degradation problem caused by LCD subpixels, the simple and useful method is gap control method [70]. By locating lens array not at the focal length from display panel but a little bit closer or further, color separation problem can be reduced as shown in Fig. 3.5(b). In the implemented real-time 3D visualization system, this method was also applied in 3D display stage by setting gap a little bit larger than the focal length.

However, this method causes another image degradation problem. Since the elemental image is generated as focal mode, which means that the gap is assumed as the exact focal length, the display lens array should be that much apart from display panel. However strictly speaking, the gap control method is for the real or virtual mode integral imaging, therefore the central depth plane is fixed and the depth region is limited around the central depth plane [16]. Hence, although the theoretical expressible depth range of focal mode integral imaging is infinite, practically the depth range is limited by quantized subpixel pitch. If the pixel pitch can be infinitesimal, the color separation problem becomes solved, and the expressible depth range goes to the infinite.

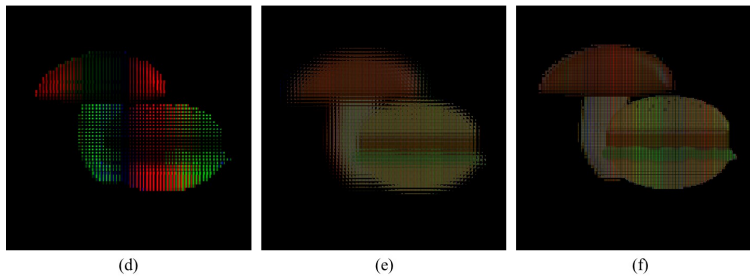
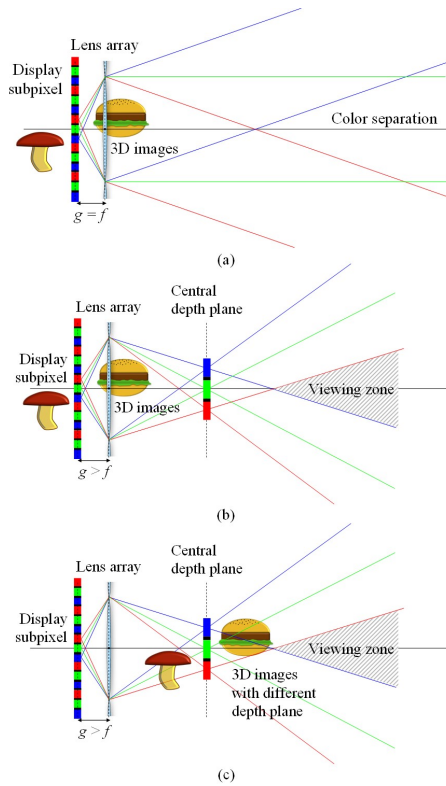


Figure 3.5 Principles of gap control method with depth plane adjustment method: (a) color separation problem in integral imaging, (b) gap control method, (c) gap control method with depth plane adjustment, (d) simulation result of color separation ($g = f$), (e) gap control method ($k = 0, g = 1.5f$), and (f) gap control method with depth plane adjustment ($k = 1, g = 1.5f$).

This image degradation problem can be reduced by adjusting the relative position of display lens array and the 3D objects. By locating 3D objects around the central depth plane, the expressible depth range could be fully utilized. For example, although the 3D objects are quite apart from lens array at pickup stage as shown in Fig. 3.3(a), the reconstructed 3D images can be located around lens array at display stage by adapting pixel mapping algorithm as shown in Fig. 3.3(d). By using this method, 3D images were reconstructed around central depth plane, and the image degradation problem can be resolved. Figure 3.5(c) shows an example of gap control method with depth plane adjustment. This method may not be effective for the 3D objects with large depth differences. However, this method is valid for most cases whose scale of objects is similar to the depth differences.

Figures 3.5(d)-3.5(f) are simulation results to verify the gap control method with depth adjustment. For the simulation, an integral imaging simulator based on MATLAB was used. This simulator contains the information of subpixel structures of LCD panel to verify color separation problem of proposed system. Simulation condition is identical to the implemented system, and the specification is shown in Table 3.1. The gap is set to $1.5f$ (4.85 mm) which is one of the reasonable values for the gap control method because the thickness of lens array is already $1.0f$ (3.3 mm). Therefore, the central depth plane is located at 9.9 mm in front of lens array, and the 3D images can be located closer to the central depth plane when k is 1. Note that the implemented situation is quite different from the diagram in scale shown in Figs. 3.2 and 3.3. Without gap control method, color separation problem which makes 3D images hard to recognize is severe as

shown in Fig. 3.5(d). By applying gap control method, image quality is clearly improved as shown in Fig. 3.5(e). However, the result image is still blurred and sliced at borders because of the limited depth range of real mode integral imaging. By applying depth plane adjustment to gap control method, the image is clearer and not much blurred as shown in Fig. 3.5(f). Therefore, the simulation results show the validity of proposed gap control method with depth plane adjustment. This gap control method with depth plane adjustment proposes a guideline to select proper k value. Beyond the real-time issues of pseudoscopic-orthoscopic conversion algorithm, this algorithm can provide real-time 3D images without any image degradation caused by gap control method.

Table 3.1 Specifications of real-time 3D visualization system based on light field imaging and integral imaging system.

Lens array (Pickup)	Lens pitch	1 mm
	Focal length	3.3 mm
Lens array (Display)	Lens pitch	1 mm
	Focal length	3.3 mm
CCD	Pixel pitch	5.5 μ m
	Resolution	2336 \times 1752
	Frame rate	32 Hz
Display panel	Pixel pitch	0.1245 mm
	Resolution	3840 \times 2400
Gap		4.95 mm

Experimental setup of real-time capturing and 3D visualization system is implemented with lens array pickup system and integral imaging display system. A high frame rate CCD and a lens array are used for lens array pickup system, and an LCD panel and an identical lens array are used for integral imaging system. Figure 3.6 shows the implemented real-time capturing and 3D visualization system. For the real-time capturing and 3D visualization a high frame rate CCD from Allied Vision Technology (Prosilica GX2300C) and a desktop (Intel i7 processor with NVIDIA GTX 470 graphic card) were used, and for the high quality 3D visualization a high resolution LCD panel (IBM 22-inch 3840×2400) was used. Real-time pixel mapping algorithm is implemented only with open CV programming without any GPU programming. The identical 1mm lens arrays with 3.3mm focal length were used for both pickup and display. Detailed specification is listed in Table 3.1.

Since the proposed system is composed of several sensitive optical devices, the calibration problem is a practical issue for the implementation. At first, pickup lens array should be calibrated with CCD, and then the start pixel should be found because real-time pixel mapping algorithm has to receive start pixel as an initial input; otherwise it cannot be performed correctly. The display lens array should be calibrated with the displayed elemental image also. Furthermore, one pixel in the CCD should be in one to one correspondence with one pixel in the LCD panel, because image resizing procedure takes time and it is hard to satisfy real-time condition with a desktop. Therefore, two rulers were used to match pickup world and display world in the same scale.

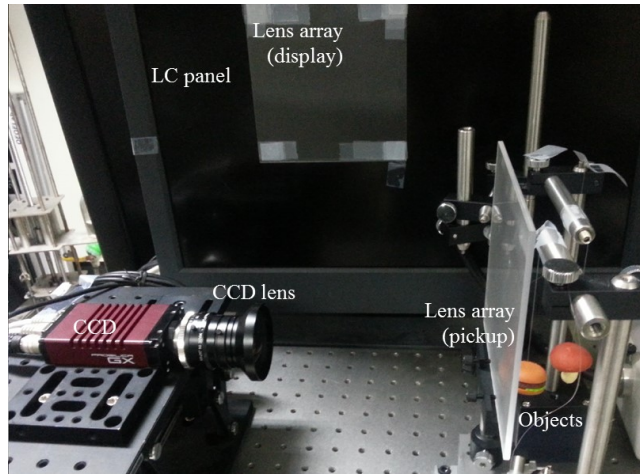


Figure 3.6 The implemented real-time 3D visualization system based on lens array pickup and integral imaging.

With the implemented system, 3D visualization experiments are presented. Figure 3.7 shows experimental result. The parallax within viewing angle is clearly provided as shown in Fig. 3.7(a). The real-time pixel mapping algorithm is applied so that the reconstructed 3D images contain orthoscopic depth information. The hamburger object is at the front not only in pickup stage, but also in display stage. To verify real-time capturing and 3D visualization, 3D objects and 3D images were recorded together as shown in Fig. 3.7(b), and swung the mushroom object. The result shows that 3D objects and 3D images are synchronized and it is real-time system. The resolution of one frame is over ultra-high definition (UHD, 3840×2400). Calculation time for one frame is about 50 ms, and the 3D images are provided up to 20 frames per second. Figure 3.7(c) shows that implemented system provides details of 3D objects very well including human hand.

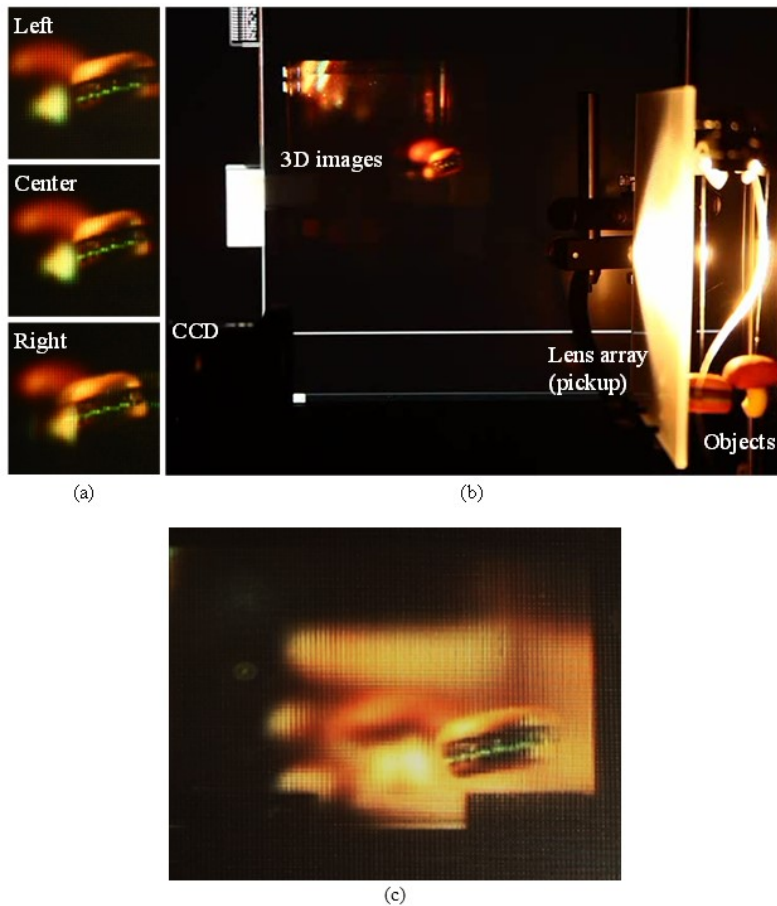


Figure 3.7 Experimental results of real-time 3D visualization system: (a) left view, center view, and right view of reconstructed 3D images, (b) real-time 3D visualization of objects, and (c) reconstructed 3D image of 3D objects and a human hand.

Furthermore, to verify gap control method with depth plane adjustment, experiments are performed with different k values. Figure 3.8 shows result images with different k values. When k is 1, central depth plane is located around hamburger object so that Fig. 3.8(a) shows high quality of hamburger

image and blurred mushroom image. However when k is 2, central depth plane is located around 1 cm behind mushroom object so that Fig. 3.8(b) shows similar quality of mushroom images and poor quality of hamburger image. In this case, optimal k value would be 1, and this result shows that the gap control method with depth plane adjustment is valid and improves image quality. Furthermore, since depth planes are adjustable instantly in any time, the observer can find optimal depth plane to watch.

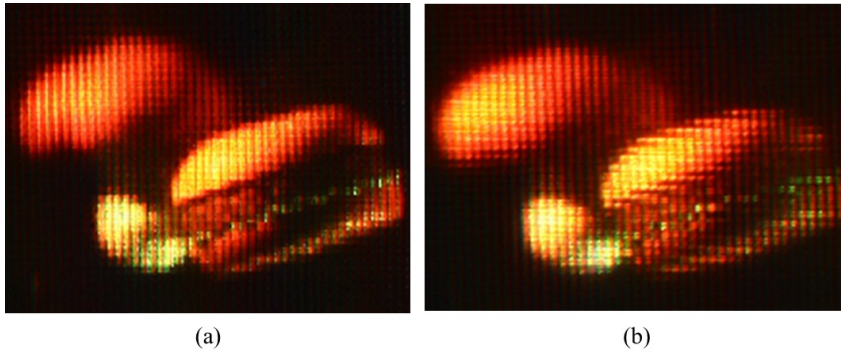


Figure 3.8 Experimental results of proposed real-time capturing and 3D visualization system with different k values: (a) when central depth plane is located around hamburger object ($k = 1$) and (b) when central depth plane is located 1 cm behind mushroom object ($k = 2$).

3.4 Real-time integral imaging system for light field microscopy

Beyond the real-time 3D visualization of real-scale objects, the micro-scale 3D objects can be reconstructed in real-time via a light field microscope, an integral imaging system, and the real-time elemental image generation algorithm. In this chapter, a real-time integral imaging system was presented for light field microscopy [10–13]. Figure 3.9 shows a schematic diagram of the proposed system. A light field microscope captures the light field information of the micro-scale objects as shown in Fig. 3.9(a), and by locating captured pixels at the proper position of an elemental image, a real and orthoscopic 3D image can be obtained, as shown in Fig. 3.9(b). The observer can also instantly adjust the depth plane of the reconstructed 3D image by changing the parameters in the real-time elemental generation algorithm.

Unlike the real-scale version, this system utilizes different micro lens arrays at the capturing stage and the display stage. Therefore, the careful considerations on the scale and the directional information are required to provide the undistorted 3D images. Since the pitch of the display lens array is usually bigger than that of the micro lens array in light field microscope, a reconstructed 3D image is magnified not only by magnification of the objective but also by the lens array difference. With the assumption that the number of sensor pixels is equal to the number of display pixels, a lateral magnification factor M_{xy} is derived by multiplication of the lens size difference and objective magnification as follows:

$$M_{xy} = M_o \times \frac{p_d}{p_c}, \quad (3.3)$$

where M_o is the magnification of objective, p_d is the lens pitch of the display lens array, and p_c is the lens pitch of the micro lens array in the capturing stage.

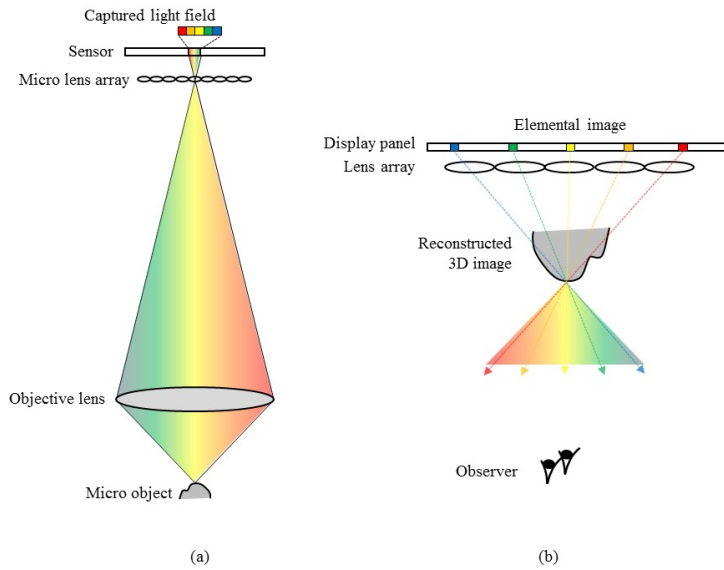


Figure 3.9 The schematic diagram of the real-time integral imaging system for light field microscopy: (a) light field capturing with a light field microscope and (b) 3D image reconstruction using an integral imaging system.

However, the axial magnification factor M_z is determined by the lateral magnification factor and the angular resolution. Since the maximum angle of the light field cone is determined by the numerical aperture (NA) of the objective lens in light field microscope, the NA of the lenses in the display

lens array should be equal to that of objective lens in order to reconstruct right depth information. Here, M_z is derived as follows:

$$M_z = M_o \times \frac{p_d}{p_c} \times \frac{NA_o}{NA_d}, \quad (3.4)$$

where NA_d and NA_o are the NA of the display lens array and objective lens in light field microscope, respectively. In practice, the NA of an individual lens in a display lens array is much lower than that of the objective lens. Therefore, the depth information of the reconstructed 3D image is distorted unless additional image processing is applied.

To reconstruct a 3D image of a micro object without distortion, the careful consideration of the f-number is required. The f-number of a lens (F) is defined as follows:

$$F = \frac{f}{p} = \frac{1}{2NA}, \quad (3.5)$$

where f is the focal length and p is the diameter of the lens. As mentioned above, the NAs of the objective and display lens array are usually different, so the f-number of them should be matched by image processing. As mentioned above, in practice, it is much more difficult to make a high NA lens array than to make a high NA objective. Therefore, only a fraction of the captured information can be optically reconstructed as a 3D image. However, expressing the light field of a micro object without distortion is important, in terms of examining the 3D shape of an object, and the f-number matching method can provide undistorted 3D information to experimenters.

Figure 3.10 shows an example of the light field of *c.elegans* captured by the light field microscope system. a 40×/0.65NA objective, a Fresnel Tech. 125 μm micro lens array with 2.5 mm focal length, Olympus BX53T optical

microscope and AVT Prosilica GX2300C CCD were used to build a light field microscope system. In Fig. 3.10, the red lines indicate the micro lens array border, yellow circles show the circular aperture of the objective, and the sky blue rectangles indicate the region that can be expressed with a typical 1 mm lens array with the 3.3 mm focal length used in integral imaging. Detailed specifications for the implemented system are listed in Table 3.2. Due to the mismatch between the image-side f-number of the objective and the f-number of the micro lens array, the outer region of the sensor cannot receive a light field signal [10], and the circular aperture stop inside the objective lens forms an array of image circles. However, the expressible region is only a small part of the captured light because of another f-number mismatch between the objective and the display lens array as shown in Fig. 3.10. Fortunately, the resolution of CCD is usually much greater than the resolution of the display device so that the light field information is enough to generate the elemental image. The resolution of the captured image for a single lens is 31×31 . However, the display panel pitch is $125 \mu\text{m}$ and the pitch of the display lens array is 1 mm. Therefore, the resolution of a single elemental image is 8×8 , so the elemental image is generated by undersampling. Therefore, the resolution of the reconstructed 3D image can be improved by cropping wasted regions such as black regions due to the circular aperture before the undersampling process. Nevertheless, the captured light field should be stored for full-resolution post-processing regardless of the elemental image generation method used.

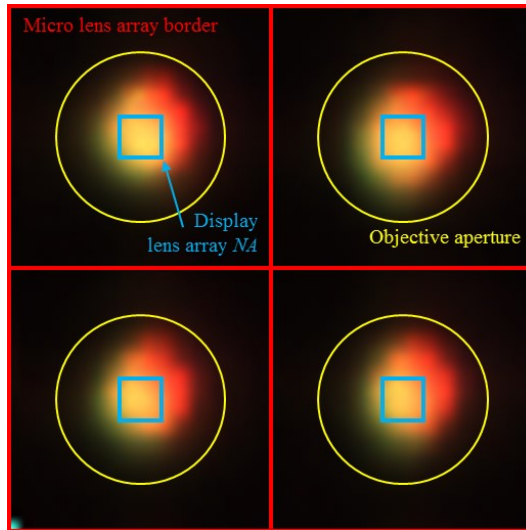


Figure 3.10 part of captured light field of *c.elegans* with a light field microscope with $40\times/0.65$ NA objective, Fresnel Tech. $125\ \mu\text{m}$ micro lens array (focal length $2.5\ \text{mm}$): (red) 2 by 2 micro lens array region, (yellow) objective aperture stop, (sky blue) region that can be expressed with display lens array ($1\ \text{mm}$ lens array with $3.3\ \text{mm}$ focal length).

To generate an accurate elemental image from a captured light field, only the sky blue regions in Fig. 3.10 would be used; otherwise the reconstructed 3D image is distorted in depth. Therefore, the sky blue region should be cropped first. Figure 3.11 shows the principle of the elemental image generation process with one part of captured light field. Figure 3.11(b) shows the rearranged image with the cropped images. The pixel mapping algorithm is then applied to the rearranged image to produce a real and orthoscopic 3D image without pseudoscopic problems. As mentioned above, the depth plane can be adjusted by changing the algorithm parameter k in the elemental image generation algorithm [45–48].

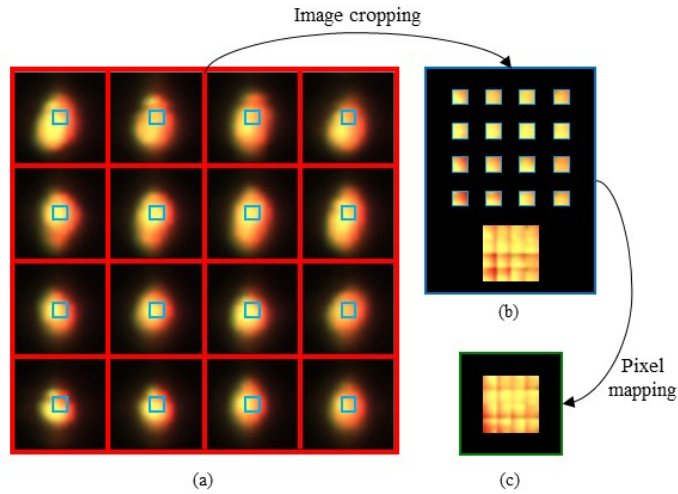


Figure 3.11 The elemental image generation from a captured light field with f-number matching: (a) a part of the captured light field with LFM, (b) rearranged image by cropping image regions that can be expressed with the display lens array, and (c) generated elemental image using the pixel mapping algorithm ($k = 0$).

In this study, the parameter k was set to zero, which is the simplest way to solve the pseudoscopic problem: rotating each elemental image by 180 degrees. This method was introduced earlier by Okano *et al.* in conjunction with a real-time display [8]. However, this algorithm provides only virtual orthoscopic images with the conventional lens array pickup system, because the pickup system is capable of capturing 3D objects only behind the lens array. However in the light field microscope system, the micro lens array captures the light field relayed by the objective lens, and the experimenter can easily adjust the focal plane relayed with the objective lens by moving the stage up and down. Therefore, the use of zero for the algorithm parameter

k is the best for the proposed system, because it is not necessary to adjust the depth planes with post processing. Orthoscopic 3D images are obtained as both virtual and real images by rotating each elemental image.

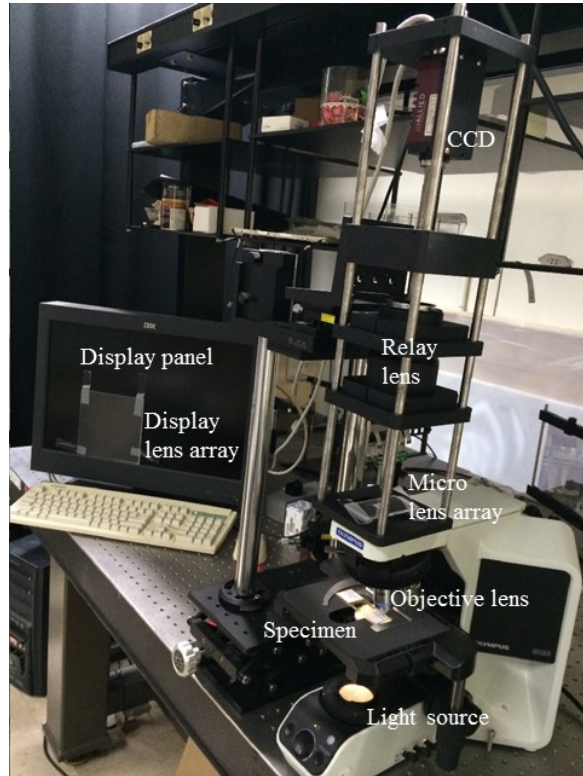


Figure 3.12 The implemented real-time integral imaging system for light field microscopy.

Figure 3.12 shows the implemented real-time integral imaging system for light field microscopy. An incoherent light source is located at the bottom, transmitted to the micro object, and imaged by a micro lens array. In practice, a relay lens (Canon EF 100 mm f/2.8 Macro USM) is used to image the light

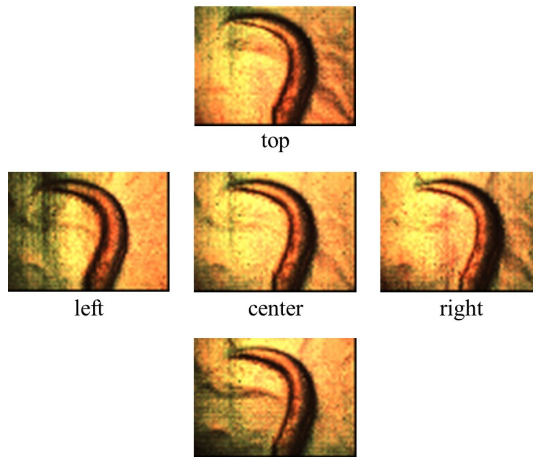
field from the micro lens array to the CCD sensor, as shown in Fig. 3.12. The captured light field information is transmitted to the desktop at a 32 frame per second (FPS). Therefore, half of the captured images are used for elemental image generation because the implemented elemental image generation algorithm is capable of providing only about 16 FPS. For integral imaging, a high resolution LCD (IBM 22 inch 3840×2400) and a 1 mm lens array with a 3.3 mm focal length are used, as listed in Table 3.2.

Table 3.2 Specifications of the implemented real-time integral imaging system for light field microscopy.

Micro lens array (Pickup)	Lens pitch	125 μm
	Focal length	2.5 mm
Objective lens	Magnification	40 \times
	NA	0.65
Lens array (Display)	Lens pitch	1 mm
	Focal length	3.3 mm
CCD	Pixel pitch	5.5 μm
	Resolution	2336 \times 1752
	Frame rate	32 Hz
Display panel	Pixel pitch	0.1245 mm
	Resolution	3840 \times 2400



(a)



(b)

Figure 3.13 Experimental results for the implemented light field microscope: (a) the captured light field image of *c.elegans*, (b) perspective views extracted from captured light field image.

With the implemented system, the real-time integral imaging experiment was presented. At first, the implemented light field microscope system was verified with a moving micro object. Figure 3.13(a) shows a captured light field image of *c.elegans* [73–75]. The captured image is

composed of circular light field images, as expected. Perspective views are extracted from the captured light field image, as shown in Fig. 3.13(b). These results are in agreement with previous studies on light field microscopy [11–15].

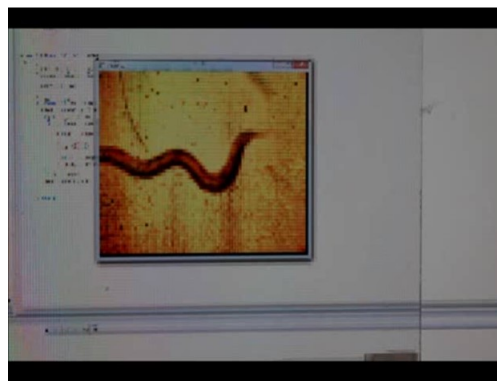
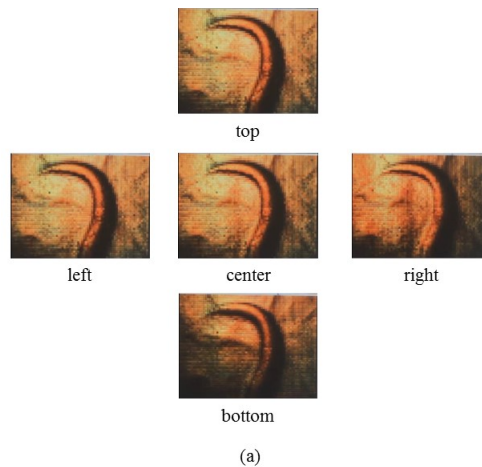


Figure 3.14 Experimental results for the proposed real-time integral imaging system for light field microscopy: (a) perspective views of reconstructed 3D images and (b) the conceptual video of real-time 3D experiment.

With the captured light field image, an integral imaging experiment was presented. Figure 3.14(a) shows the perspective views of reconstructed 3D images with the generated elemental image. The developed system provides an orthoscopic 3D image in real-time. By using this real-time characteristic of the proposed system, real-time 3D experiments can be performed. Figure 3.14(b) shows the conceptual experiment for the proposed 3D experiment. The experimenter observes a micro object in 3D and in real-time, and instant feedback with the microscope is possible. Due to the multiple viewpoints characteristics of integral imaging, multiple experimenters can observe the moving micro object in the microscopic experiment.

3.5 Conclusion

In this chapter, the real-time elemental image generation algorithm and the real-time 3D visualization systems for the real-scale and the micro-scale were presented. The integral imaging system could provide the real and orthoscopic 3D images by rearranging the pixel values of the captured images. Based on this algorithm, the system could provide a real-time 3D images of a real-scale object using a lens array pickup system and an integral imaging system. In addition, the real-time 3D images of a micro-scale object could be reconstructed in real-time using a light field microscope and an integral imaging system. The depth plane adjustment method and the f-number matching problems in the systems were analyzed to provide 3D images in the best quality. The simulation results and the experimental results were presented to verify the idea.

By the way, these systems could not overcome the basic limitation of light field imaging or integral imaging. The lateral resolution of the captured 3D information and the reconstructed 3D images were too low compared to the state-of-art 3D imaging devices and 3D display devices, respectively. Several lens array shifting approaches were introduced to enhance the lateral resolution [14, 15], but those could not provide real-time 3D images due to the multiple shots. To achieve the high resolution 3D images while maintaining the one-shot characteristics, a new capturing method and its display pair are required.

Chapter 4 . Real-time 3D visualization method based on dual-dimensional imaging

4.1 Introduction

For the resolution improvement in light field imaging, various approaches have been introduced for decades. The 2D camera arrays could capture the high resolution light field images with one-shot imaging, but it requires detailed calibration and a large space [7]. The multiple shots of light field imaging with the lens array shifting can provide high resolution 3D information in a camera [14, 15]. However, it lost the one-shot characteristics and could not be utilized in real-time 3D visualization systems. The beam splitters with the multiple light field imaging devices can obtain the higher resolution, but the one beam splitter can only double the resolution which is still low compared to the competing technologies [76].

In this chapter, a high resolution light field imaging system called dual-dimensional imaging is proposed. A dual-dimensional imaging system captures 2D image and light field image simultaneously using a beam splitter inside the capturing beam path. The obtained 2D and 3D information can be fused as a high resolution light field images in the light field spectral domain

based on the Fourier slice photography theorem. The resultant high resolution light field is reconstructed via a light field display which is built with stacked LCDs. The whole procedure including the light field upsampling and the layer image generation is done in real-time with the parallel computation [44].

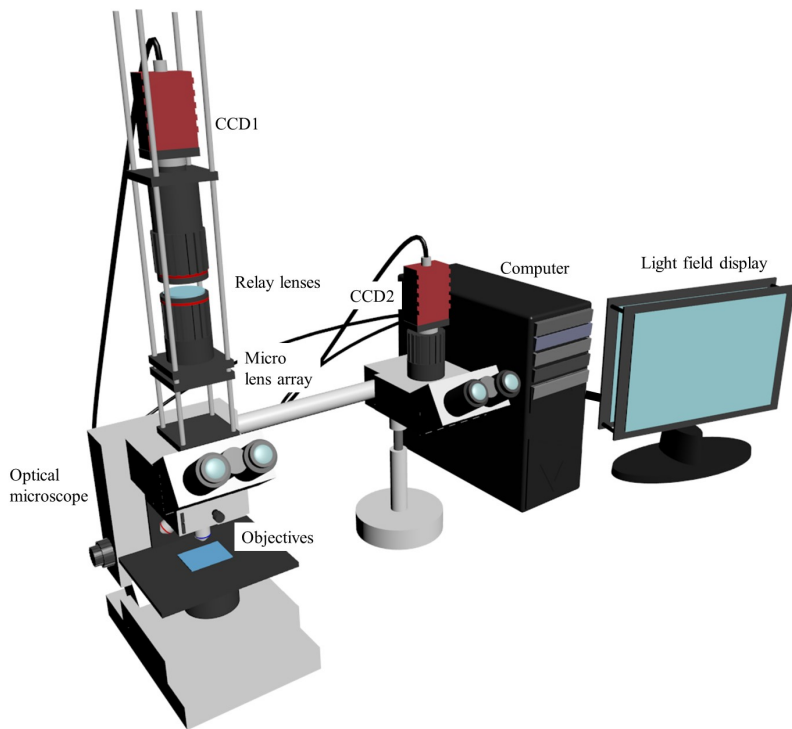


Figure 4.1 The schematic diagram of the real-time 3D visualization system based on dual-dimensional imaging and a light field display.

Figure 4.1 shows the schematic diagram of a real-time 3D visualization system based on dual-dimensional imaging and computational light field display. With this system, one can observe the living cells in 3D and in real-time, record the whole 3D information videos, and track the living organism with the microscope stages. In Chapter 4.2, the principles and the implementation of the dual-dimensional imaging system and the light field upsampling algorithm are presented. The 3D visualization of the obtained information using a light field display is introduced in Chap. 4.3.

4.2 Dual-dimensional imaging

4.2.1 2D/3D simultaneous imaging

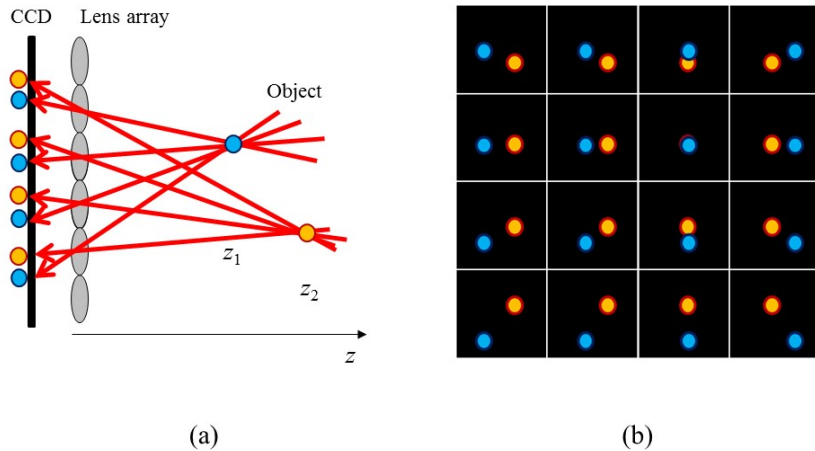


Figure 4.2 The example of the light field imaging of the two points: (a) The schematic diagram of the light field imaging system and (b) The captured light field image.

Dual-dimensional imaging is to capture a 2D image and light field image simultaneously, and to generate the upsampled light field from them. Previously, a high resolution light field imaging method was introduced by Lu *et al.*, which provides upsampled light field from a 2D and a light field images [77]. However, their method was based on not simultaneous but sequential capturing, and their algorithm was not in real-time. In this dissertation, the dual-dimensional imaging system is proposed which captures 2D and light field image simultaneously with a beam splitter, and

the real-time light field upsampling algorithm is introduced based on Fourier slice photography theorem [78, 79].

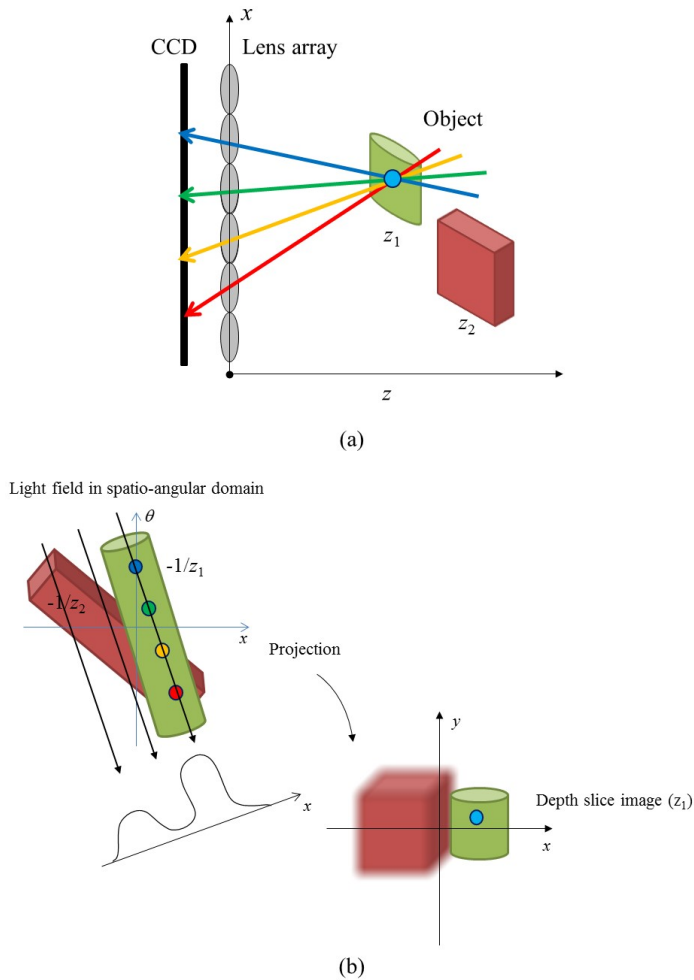


Figure 4.3 The principle of the light field analysis and generation of the depth slice image: (a) The light field imaging system of the two plane objects and (b) The captured light field in spatio-angular domain and the depth slice image generated with the light field projection.

Fourier slice photography theorem is about how to deal with the light field information in Fourier spectral domain [78]. Figure 4.2 shows an example of light field imaging of two objects in different depth planes. Note the 2D light field (x, θ) is assumed for the simplicity and it could be expanded to four-dimensional (4D) light field easily. As shown in Fig. 4.2(b), the perspective images are obtained, and the parallax of the closer object is larger than that of the farther object. By calculating the corresponding points between images behind the nearby lenses, the depth information can be extracted [9]. However, since this method is based on the color value of each pixel, the algorithm is time-consuming and the error depends on the texture.

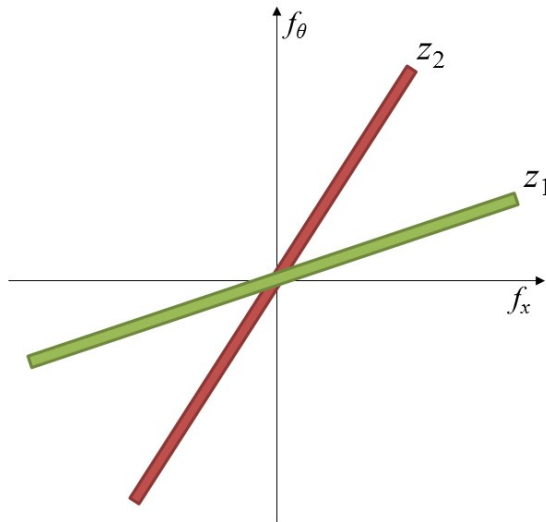


Figure 4.4 The principle of the Fourier slice photography theorem : The light fields that are started from a certain depth form a line with the slope z in spectral domain.

However, in light field domain, the depth slice image can be obtained in real-time. Figure 4.3 shows the principle of depth slice image generation in light field domain. The light field started from a point at depth z_1 is recorded on CCD through the lens array. As shown in Fig. 4.3(b), these light fields form a line with slope $-1/z_1$ in the light field domain. Therefore, the depth slice image focused on z_1 plane can be extracted with the projection with the $-1/z_1$ direction.

In addition, the obtained light field can be analyzed in light field spectral domain. In the light field spectral domain, the light fields from different depth planes can be separated more easily. Figure 4.4 shows the light field spectrum of the captured light field in Fig. 4.3. Since the light fields from the same depth plane form lines with the identical slope, they are located on a line in the light field spectral domain. For example, the light fields from depth z_1 form a line $f_\theta = z_1 \times f_x$ in light field spectral domain. This principle is called Fourier slice photography theorem, and the depth slice image or the all-in-focus image can be generated faster with this principle [78].

Based on Fourier slice photography theorem, a dual-dimensional imaging system was proposed. Figure 4.5 shows the schematic diagram of the dual-dimensional imaging system. The light fields started from the specimen are collimated after the infinity corrected objective lens. After it, the collimated light beam is divided into two at the beam splitter. The transmitted light beam is converged after a tube lens and a light field image is obtained with a micro lens array located at the image plane and the CCD1 focuses on the back focal plane of the micro lens array. The reflected light

beam is reflected again at the mirror and converged at a tube lens, and a 2D image is recorded with the CCD2 located at the image plane. Note that the relative distance between the lens array and the tube lens is identical to the distance between the CCD2 and the tube lens. This configuration ensures that the captured 2D image is an image focused on the lens array plane ($z = 0$). According to the Fourier slice photography theorem, the Fourier spectrum of the 2D image forms a line ($f_\theta = 0$) in the light field spectrum domain. Therefore, this dual-dimensional imaging system can provide the upsampled light field in real-time. The resultant maximum lateral resolution of the upsampled light field is same as that of the conventional optical microscope while the depth of field is same as that of the light field microscope.

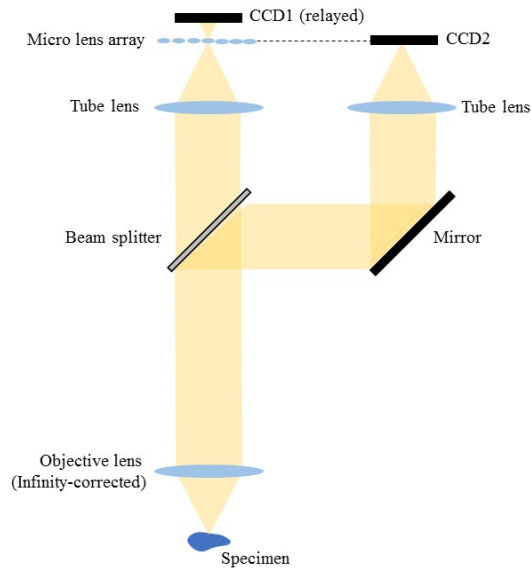


Figure 4.5 The schematic diagram of the dual-dimensional imaging system.

4.2.2 Light field upsampling in dual-dimensional imaging

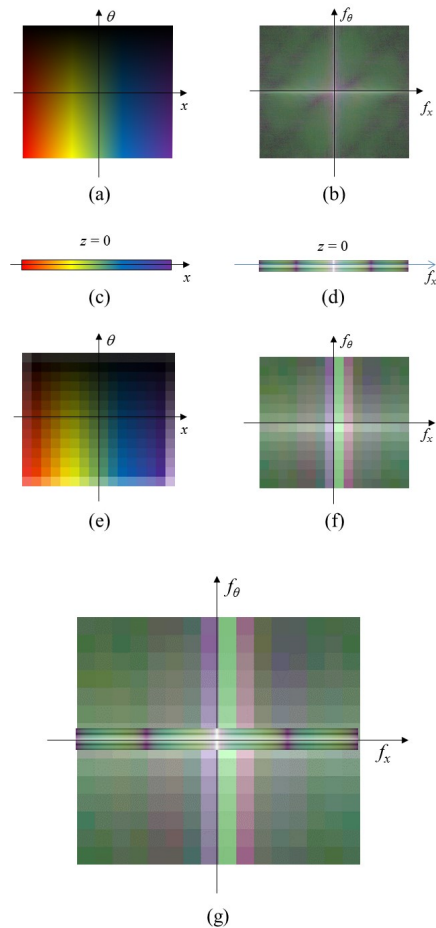


Figure 4.6 The principle of light field upsampling in dual-dimensional imaging system: (a) Original light field, (b) Original light field spectrum, (c) Captured 2D image, (d) 2D Fourier transform of captured 2D image, (e) Captured light field, (f) 4D Fourier transform of captured light field, and (g) Spectrum of upsampled light field. Note that the line $f_{\theta} = 0$ in the light field spectrum domain is substituted to (d).

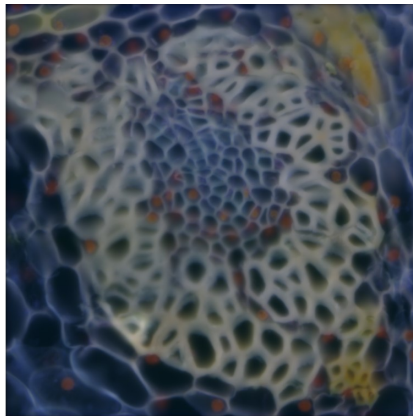
Table 4.1 Specifications of the light field upsampling simulation in dual-dimensional imaging system.

Micro lens array	Lens pitch	125 μm
	Focal length	2.5 mm
Objective lens	Magnification	20 \times
	NA	0.5
CCD	Pixel pitch	8.3 μm
	Resolution	900 \times 900
3D data from confocal microscope (Convallaria)	3D scale	375 \times 375 \times 31 μm
	Resolution	900 \times 900 \times 31
Simulation wavelength		532 nm

Based on the Fourier slice theorem, the light field could be upsampled in the dual-dimensional imaging system. Figure 4.6 shows the principle of the light field upsampling. Suppose the original light field and the light field spectrum of a sample is Figs. 4.6(a) and 4.6(b), respectively. The captured 2D and light field images can be expressed as Figs. 4.6(c) and 4.6(e), respectively. Since the 2D image is focused on the $z = 0$ plane, the Fourier spectrum of 2D and light field images can be interpreted as Figs. 4.6(d) and 4.6(f), respectively. Note that the Fourier spectrum of the 2D image forms the $f_\theta = 0$ line in the light field spectral domain. Therefore, by substituting the $f_\theta = 0$ layer and performing additional inverse Fourier transform, we can obtain an upsampled light field with the dual-dimensional imaging system.

Since the obtained 2D image has a higher lateral resolution than that of the light field image, the additional interpolation process is required before

the upsampling. Since the texture of the biological sample changed smoothly in lateral direction, the interpolation works appropriately. In this case, the simple zero-padding in Fourier domain was applied for the fast interpolation.



(a)



(b)

Figure 4.7 The simulation results of dual-dimensional imaging system: (a) captured 2D image and (b) captured light field image.

For the verification, the image simulation was performed. Figure 4.7 shows the simulation results of dual-dimensional imaging system. The focal stacks of *Convallaria* captured with a confocal microscopy were used for the reference. For the simulation, the point spread functions of the 2D microscope and the light field microscope were calculated [13]. The detailed simulation condition is listed in Table 4.1. As a result, a high resolution 2D image and a light field image were obtained as shown in Fig. 4.7.

The light field upsampling was performed with the simulated images. Figure 4.8 shows the simulation results of reconstructed perspective view images of dual-dimensional imaging. The original light field provided high resolution perspective images as shown in the left column while the light field captured from the light field microscope system provided low resolution perspective view images. The upsampled light field from dual-dimensional imaging system provided higher resolution perspective view images compared to the light field imaging. Furthermore, the peak-to-signal-noise-ratio (PSNR) of the upsampled light field was higher than that of light field from light field microscope. The simulation results show that dual-dimensional imaging can provide upsampled light field compared to light field imaging system.

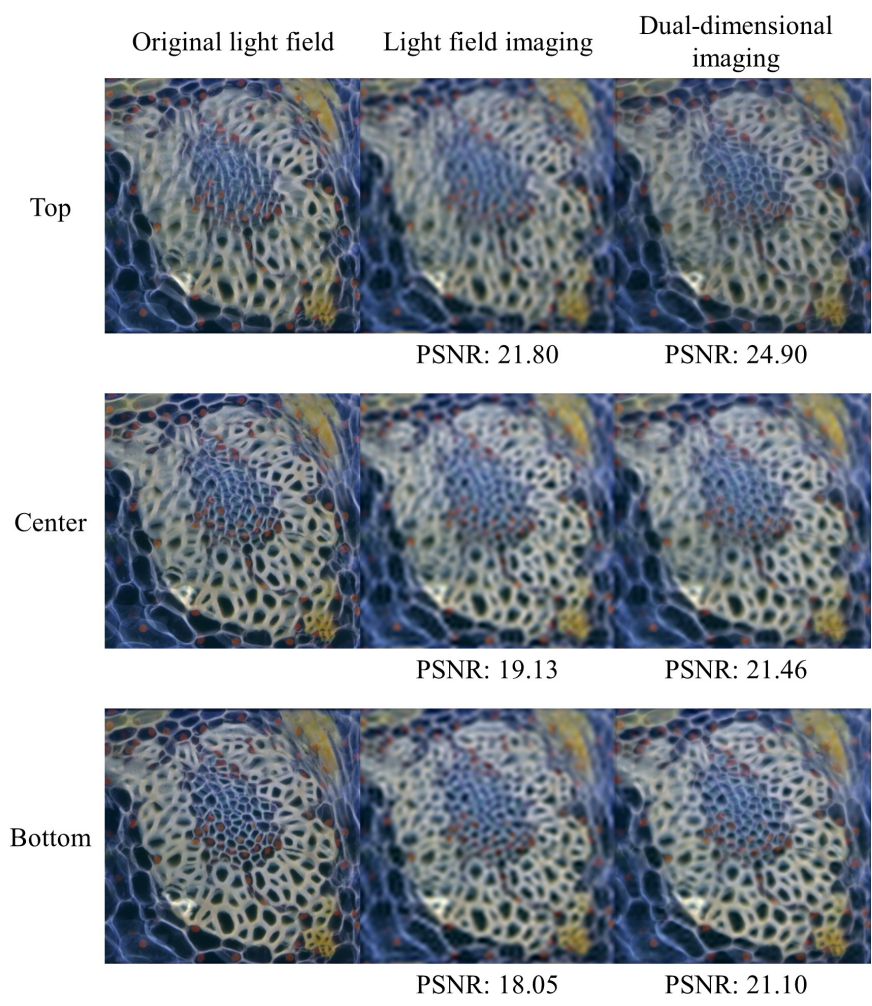


Figure 4.8 The simulation results reconstructed perspective view images of (left) original light field, (center) light field from light field imaging, and (right) light field from dual-dimensional imaging.

4.2.3 Real-time light field upsampling using parallel computation

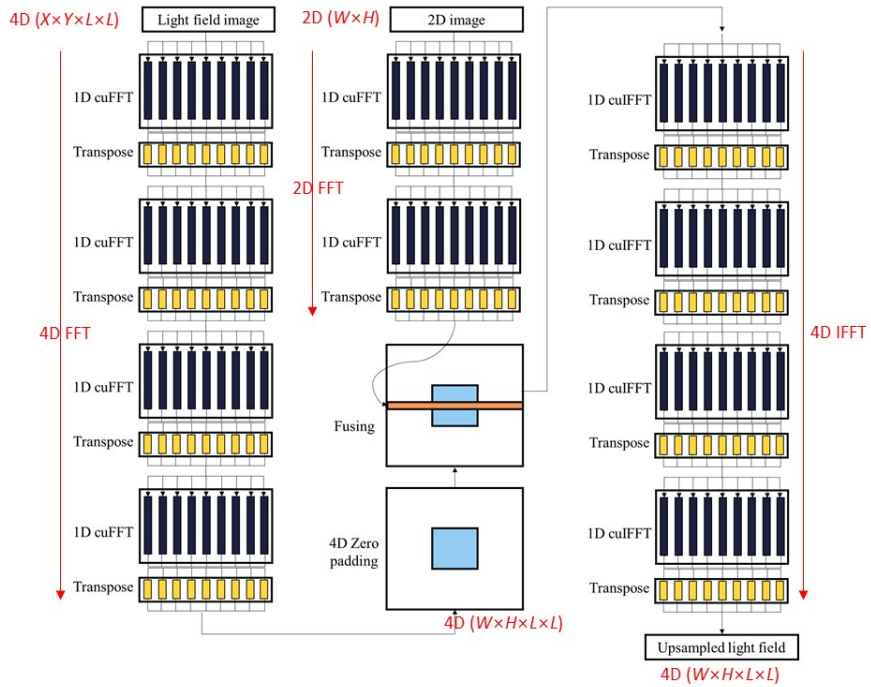


Figure 4.9 The pipeline of the real-time light field upsampling using parallel computation.

For the real-time generation of perspective views or depth slice images with dual-dimensional imaging system, the real-time light field upsampling should be accomplished. Most of the upsampling algorithm is composed of discrete Fourier transform which has a $O(n \log n)$ calculation complexity. Therefore, the real-time light field upsampling can be achieved with the parallel computation.

Figure 4.9 shows the pipeline of the real-time light field upsampling. The 1D, 2D, and 3D fast Fourier transform (FFT) algorithms for parallel computation have been implemented in compute unified device architecture (CUDA) proposed by NVIDIA which is called cuFFT [80]. Since CUDA library supports upto 3D cuFFTs, the 4D FFT or 4D inverse-FFT (IFFT) could not be achieved with the algorithms. Based on recent studies on the speed of 4D cuFFT function, the 1D cuFFT and transpose functions were used repeatedly for the 4D and 2D FFTs [81]. As shown in the Fig. 4.9, the light field image size is dramatically increased after fusing. Therefore, most of the time cost occurs at the last 4D cuIFFT part.

Figure 4.10 shows the calculation time of light field upsampling for various image size in dual-dimensional imaging with CUDA programming. Each value is the average of 100 calculations. A GTX 1080 graphic card was used in the calculation. Since most of the calculation is 4D FFT and 4D IFFT, the calculation time for an image with the 840×600 resolution was 68 seconds. However with CUDA programming, the calculation time for an image with 840×600 resolution was 151 ms. The simulation results show that the parallel implementation enabled real-time light field upsampling, and most of the time cost occurred at the 4D IFFT.

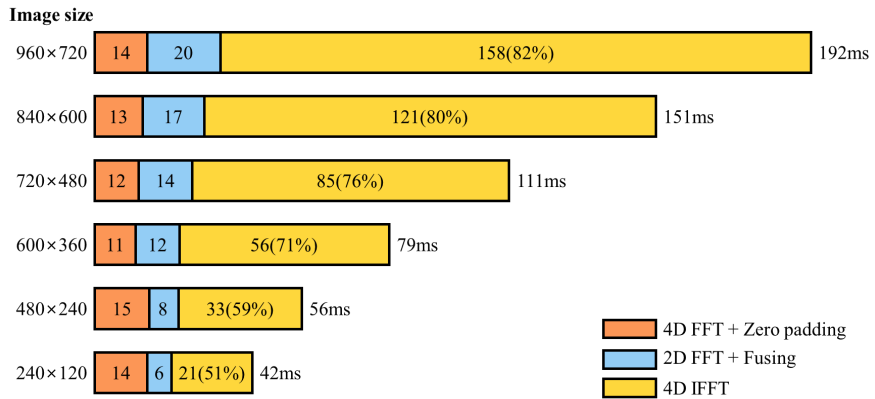


Figure 4.10 The calculation time of light field upsampling for various image size. Each value is the average of 100 calculations.

4.2.4 Experimental results

Figure 4.11. shows the implemented dual-dimensional imaging system. An Olympus BX-51T microscope and the two high frame rate CCDs were used. The beam splitter inside a side-by-side dual-view observation attachment was used for the dual-dimensional imaging scheme, which is composed of a beam splitter at the imaging path and a mirror pair as shown in Fig. 4.5. Two macro lenses were used for the relay system, and the two CCDs were synchronized with the signal generation from NI DAQ board. The detailed specifications of each item are listed in Table 4.2.

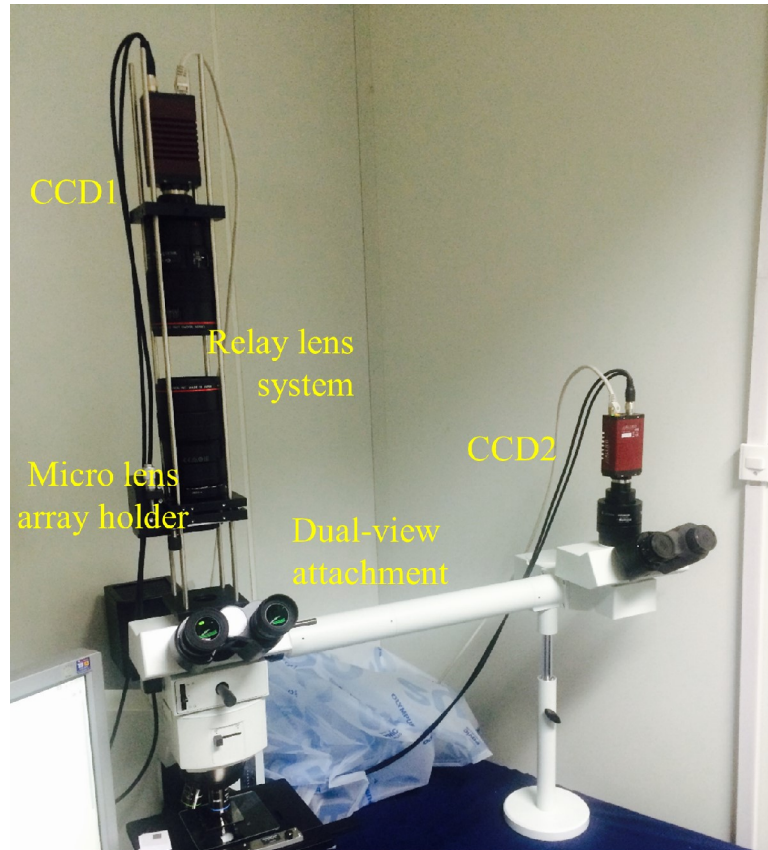


Figure 4.11 The implemented dual-dimensional imaging system.

Figure 4.12 shows the captured images with dual-dimensional imaging system. *c.elegans* was utilized as a moving sample. The proposed system could capture 2D and 3D images simultaneously as shown in Figs. 4.12(a) and 4.12(b). Practically, the capturing region could be laterally mismatched and the region of interest setting and simple image cropping should be set manually at first. Figures 4.12(c) and 4.12(d) show the light field image and the 2D image after calibration, respectively.

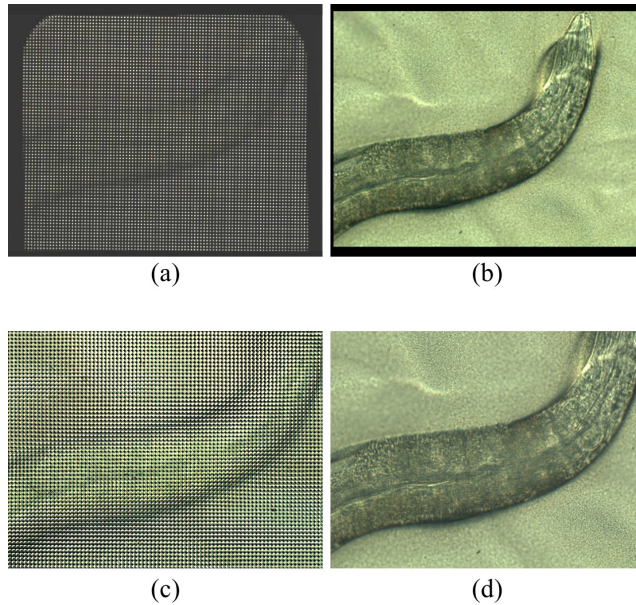


Figure 4.12 The captured images with dual-dimensional imaging system: (a) captured light field image, (b) captured 2D image, (c) light field image after calibration, and (d) 2D image after calibration.

Figure 4.13 shows the reconstructed view images using the light field image only and using the upsampled light field from dual-dimensional imaging. The experimental results show that the perspective views from upsampled light field have higher resolution and detailed information of the sample. Furthermore, the reconstructed perspective views clearly show the parallax. With the dual-dimensional system, the view videos of moving *c.elegans* were achieved. Figure 4.14 shows the reconstructed view videos using dual-dimensional imaging. The experimental results verify that the dual-dimensional imaging system can provide the real-time view videos of living cells with the improved resolution.

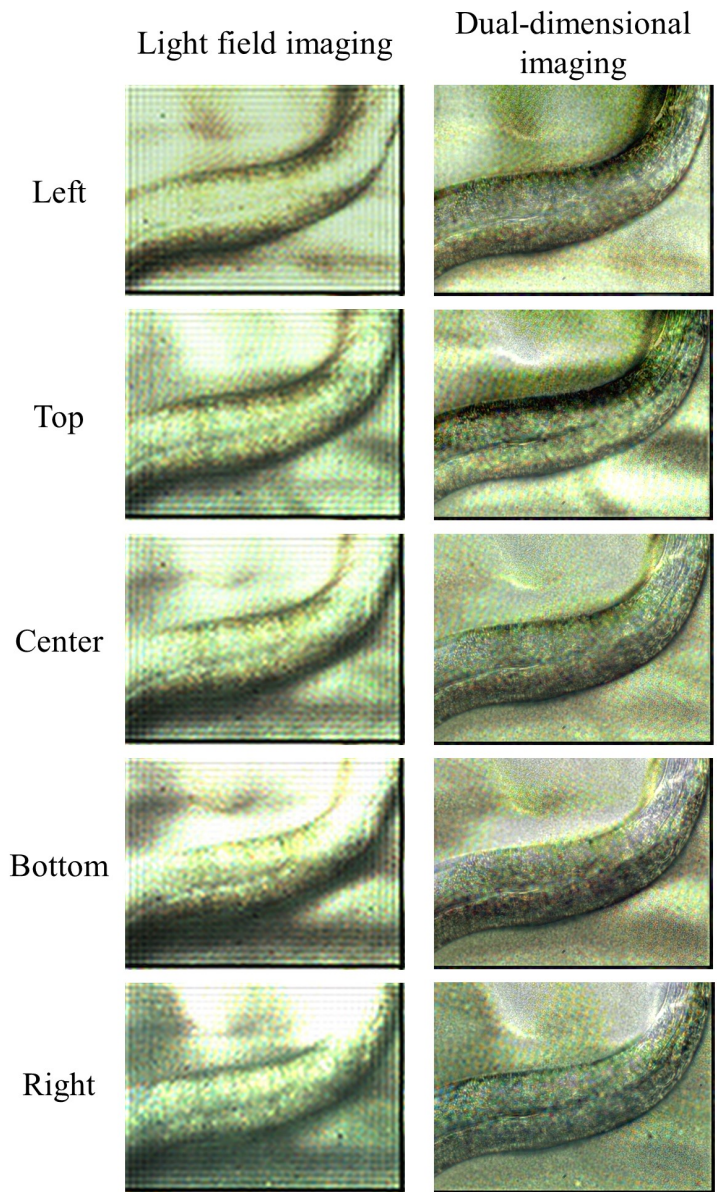


Figure 4.13 The reconstructed view images using (left) light field imaging only and (right) dual dimensional imaging.

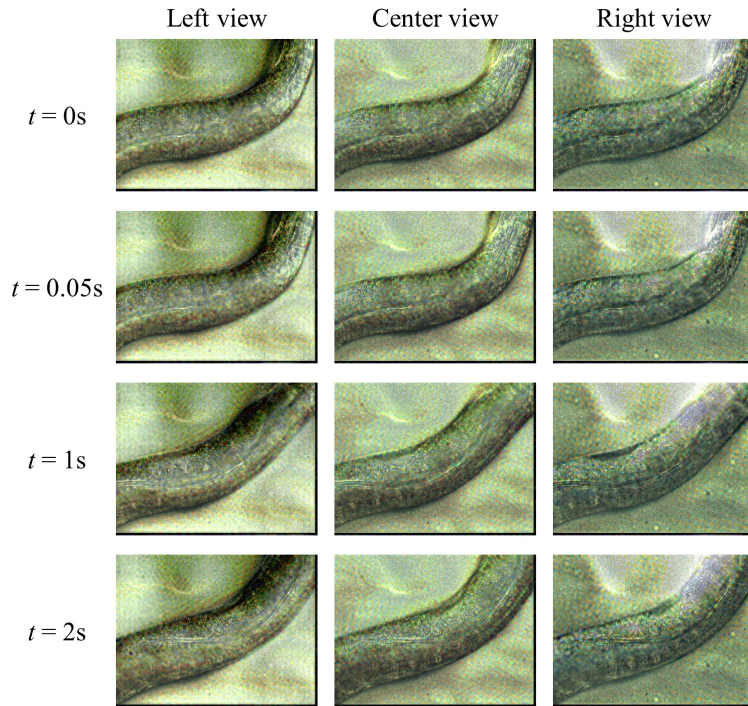


Figure 4.14 The reconstructed view videos using dual dimensional imaging.

Table 4.2 Specifications of the implemented dual-dimensional imaging system.

Micro lens array	Lens pitch	125 μm
	Focal length	2.5 mm
Objective lens	Magnification	40 \times
	NA	0.65
CCD (1 and 2)	Pixel pitch	5.5 μm
	Resolution	2336 \times 1752
	Frame rate	32 Hz
Relay lens	Focal length	100 mm

4.3 Real-time 3D visualization method based on dual-dimensional imaging

4.3.1 Light field display for dual-dimensional imaging

The upsampled light field from a dual-dimensional imaging system can be visualized in 3D with a light field display. Since the upsampled light field has a high lateral resolution, the computation stacked light field display could be used to reconstruct the light field images [40–44]. The computational light field display is based on the optimization of layer images to reproduce target light field, introduced by Lanman *et al.* [41].

Figure 4.15 shows the schematic diagram of a light field display based on stacked two in-plane switching LCDs (IPS-LCD). The incoherent light rays from the backlight unit are delivered to the observer through two LCD layers. It can be implemented without additional light source by disassembling one LCD and using the backlight unit of the other. To utilize the LCD panels without detaching the polarizer, the frontal panel is stacked upside down as shown in Fig. 4.15. The reference plane of the light field is set to the middle of two panels where the light field distribution is densest.

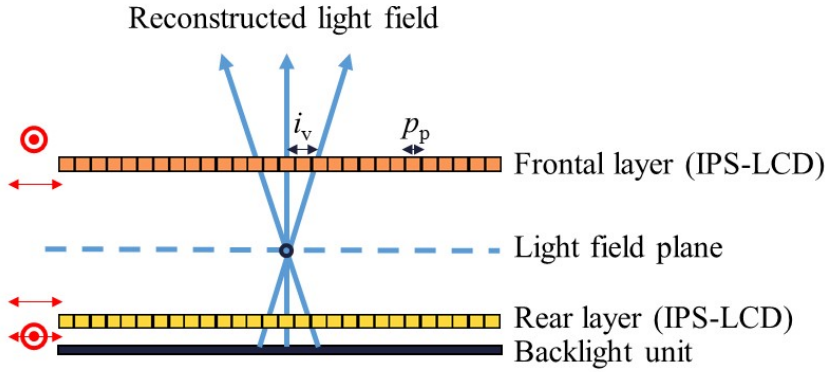


Figure 4.15 The light field display based on two stacked IPS-LCDs.

The light field reconstructed from the stacked panels can be expressed with the matrix operation. Figure 4.16 shows the principles of the matrix operations and the layer image optimization for light field display. The light field $l(i, j, s, t)$ reproduced by a pixel (i, j) of frontal panel and another pixel (s, t) can be represented as follows:

$$l(i, j, s, t) = f(i, j) \times r(s, t). \quad (4.1)$$

The whole light field distribution is the multiplication of the all possible pixel pairs within the maximum viewing angle. The matrices f and r can be expressed with $(n \times 1)$ matrix where n is the pixel number of each panel, and the contribution from each layer to the light field distribution is presented with $(mn \times n)$ projection matrices H and G , respectively as shown in Fig. 4.16(b). The contributions of each layer F and R can be derived as follows:

$$F = Hf \quad \text{and} \quad R = Gr, \quad (4.2)$$

and the reconstructed light field \tilde{L} can be expressed as follows:

$$\tilde{L} = F \odot R, \quad (4.3)$$

where \odot denotes element-wise multiplication of matrices. Note that the projection matrix is a sparse matrix which only contains 0 or 1, and the all components of the \tilde{L} , f and r are non-negative.

The layer images are optimized with the matrix factorization. When L is the target light field, the layer image optimization could be achieved by the minimization of Euclidean distance between L and \tilde{L} , as follows:

$$\arg \min_{F,R} = \frac{1}{2} \|L - FR\|^2, \text{ for } F, R \geq 0. \quad (4.4)$$

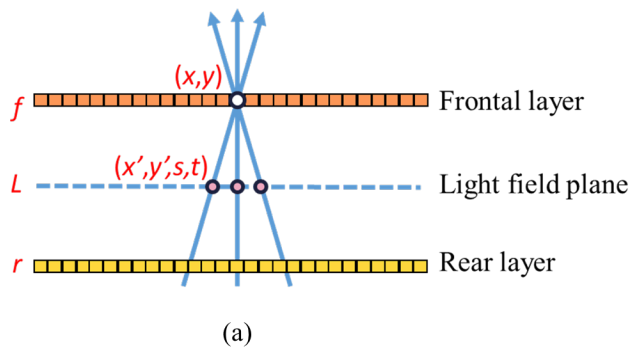
Since every component is non-negative, this least square problem can be solved with the iterative non-negative factorization algorithm [40-44]. Here, the additive update rules are applied for the factorization. Initial estimates f and r are refined as follows:

$$f = f - \frac{\Phi^T (\tilde{L} - L)}{\Phi^T \Phi} \text{ and } r = r - \frac{\Psi^T (\tilde{L} - L)}{\Psi^T \Psi}, \quad (4.5)$$

where

$$\Phi = \text{diag}(G * r) * H \text{ and } \Psi = \text{diag}(H * f) * G, \quad (4.6)$$

where the *diag* and $*$ denote diagonal operator and matrix multiplication respectively. This optimization procedure is known to be converged after around 10 iterations [40-44].



$$\begin{array}{c}
 L \qquad H \qquad f \qquad G \qquad r \\
 \left(\begin{array}{c} L(x, \theta_1) \\ x_1 \\ \vdots \\ x_m \\ \vdots \\ L(x, \theta_n) \\ x_1 \\ \vdots \\ x_m \end{array} \right) = \left(\begin{array}{c} L(x_1, \theta_1) \\ \delta_{li} \\ \vdots \\ L(x_m, \theta_n) \\ \delta_{ri} \end{array} \right) \left(\begin{array}{c} I_1(x) \\ x_1 \\ \vdots \\ x_m \end{array} \right) \odot \left(\begin{array}{c} L(x_1, \theta_1) \\ \delta_{li} \\ \vdots \\ L(x_m, \theta_n) \\ \delta_{li} \end{array} \right) \left(\begin{array}{c} I_2(x) \\ x_1 \\ \vdots \\ x_m \end{array} \right)
 \end{array}$$

Non-linear least squares problem

(b)

Figure 4.16 The layer image optimization method for light field display: (a) the schematic diagram of the light field display and (b) non-linear least squares problem of stacked light field display.

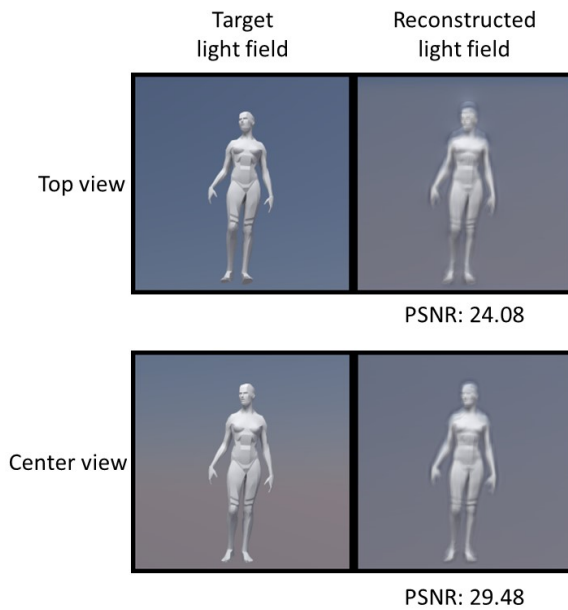


Figure 4.17 The example of the optimized layer images for the light field display.

Figure 4.17 is an example of the optimized layer images for implemented light field display. The reconstructed light field provides perspective views with horizontal and vertical parallax. Since a pixel in frontal or rear layer generates multiple numbers of light field rays within the viewing angle, the correspondence between nearby light field affects the reconstructed image quality. For example in Fig. 4.17, the background color of the top view is blue while the center view has blue and yellow background in the target light field. Therefore, the background color of the reconstructed light field is somewhat mixed for both top view and center view, and this low correspondence causes image degradation.

In dual-dimensional imaging, the in-vivo or biomedical samples are usually transparent and have high correspondence between nearby light fields. However, the image brightness might be different over directions because the intensity of the light source is directionally not uniform. This image degradation problem can be reduced by choosing proper maximum viewing angle or applying the compensation process for the image brightness correction.

4.3.2 Real-time layer image generation using parallel computation

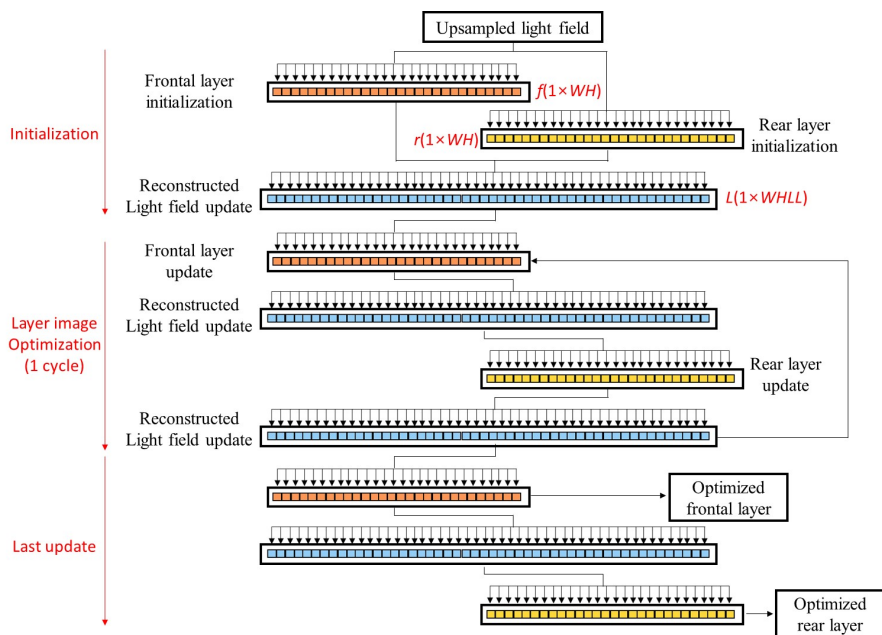


Figure 4.18 The pipeline of the real-time layer image optimization for light field display with parallel computing.

The real-time layer image optimization in the computational light field display was previously introduced by Wetzstein *et al.* [44]. In this dissertation, the identical real-time algorithm was adopted for the layer image optimization. The computation time for the layer image optimization can be dramatically reduced with the parallel computation algorithms. Since the update rule of the layer image optimization is performed layer by layer sequentially, the one update for a single layer can be done in parallel.

Figure 4.18 shows the pipeline of the real-time layer image optimization for the light field display with parallel computation. At first, each layer is initialized with certain values from the upsampled light field in dual-dimensional imaging. The initial condition could be random values between 0 or 1, or the estimation for the final layer images. Here, the initial condition was set to the center view for the fast convergence of NMF algorithm. After initialization, the layer image is optimized with the iterative update as introduced in Eq. (4.5). At each initialization and update stage, the calculation could be done in parallel because every process is independent. After iterations, the optimized frontal layer and rear layer images are obtained. In the algorithm, 5 iterations were performed for each image to obtain the real-time condition and the reasonable convergence together.

Figure 4.19 shows the calculation time of the light field upsampling and the layer image optimization for various image size. An NVIDIA GTX 1080 graphic card was used for the calculation. The whole calculation time for an image with the 800×640 resolution was 342 seconds in MATLAB and the layer image optimization part was 274 seconds (80%). However, the calculation time decreases to 225 ms for the same image with CUDA

programming and only 33% of the calculation time was for layer image optimization. Unlike 4D IFFT, each process of the layer image optimization can be completely parallelized, as shown in the simulation results. The implemented algorithm and system were able to provide 5 FPS optimized layer images with the 800×640 resolution generated from light field and 2D images captured by dual-dimensional imaging system. Note that the actual capturing was performed in 20 FPS, so the captured information contains more information than the displayed information. The calculation time and the frame rate depend on the image resolution. With the 480×240 resolution image, the system could provide 9 FPS 3D images. However, even that resolution is higher than what the integral imaging system can usually provide, which is up to 100×100 [45, 46].

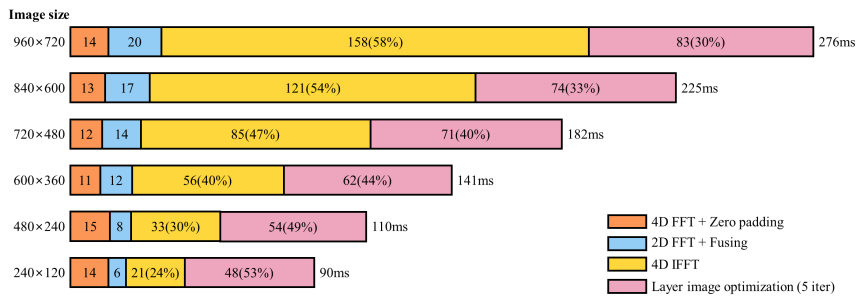
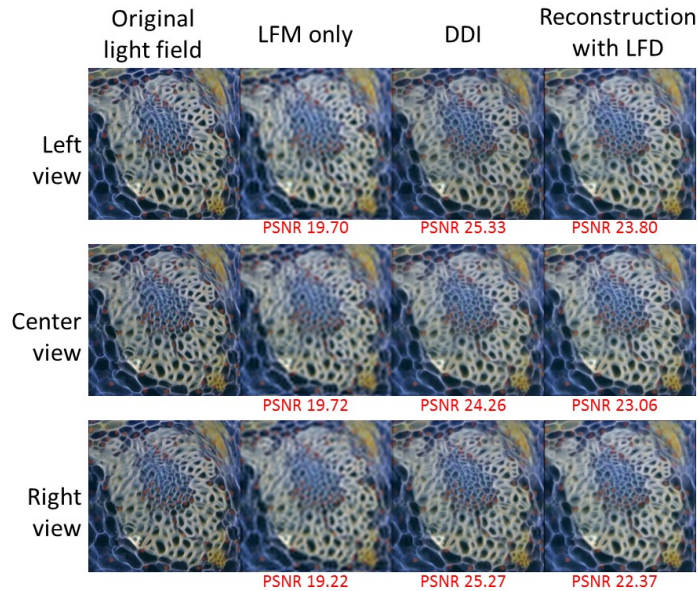


Figure 4.19 The calculation time for the light field upsampling and the layer image optimization for various image size. Each value is the average of 100 calculations.

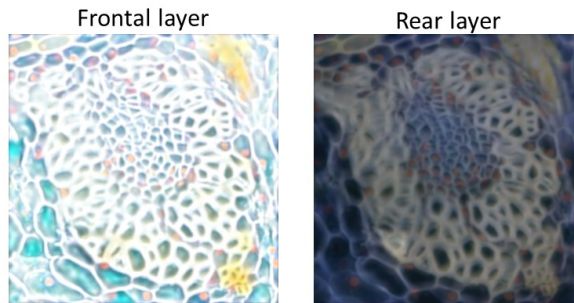
4.3.3 Simulation results

The image simulation was performed to verify the layer image optimization for dual-dimensional imaging system [82]. Figure 4.20 shows the simulation result of real-time layer image optimization. The light field display provided the perspective view images of upsampled light field information as shown in Fig. 4.20(a). The PSNR of the reconstructed image was slightly lower than that of the upsampled light field image, because of the discrete pixel structure of the light field display and the image correspondence between nearby images. Note that the PSNRs of the reconstructed view images were still much higher than those of the view images from light field microscope. This simulation result shows that the light field display can provide high resolution 3D images of dual-dimensional imaging system. Figure 4.20(b) shows the optimized frontal and rear layer images.

The layer image optimization algorithm was also applied to the upsampled light field captured with an implemented dual-dimensional imaging system as shown in Fig. 4.21. The light field display could provide the upsampled light field, but the PSNR was lower than that in the simulation results in Fig. 4.20. The lower correspondence and the non-uniform brightness may cause the image degradation. Figure 4.21(b) shows the optimized frontal and rear layer images. Note that the frontal layer is usually much brighter than the rear layer to provide high luminance light fields.



(a)



(b)

Figure 4.20 The simulation result of real-time layer image optimization: (a) reconstructed perspective view images of (left) original light field, (center-left) light field from light field imaging, (center-right) light field from dual-dimensional imaging and (right) reconstructed light field via light field display and (b) optimized layer images.

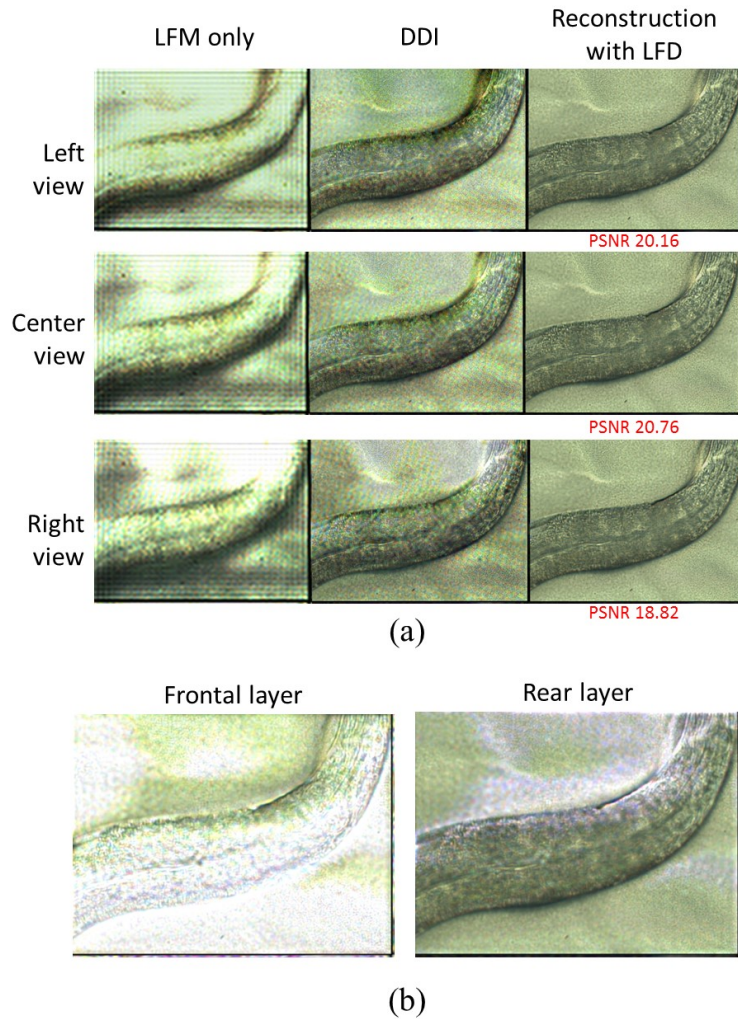


Figure 4.21 The simulation result of real-time layer image optimization with captured light field images from dual-dimensional imaging system: (a) reconstructed perspective view images of (left) light field from light field imaging, (center) light field from dual-dimensional imaging and (right) reconstructed light field via light field display and (b) optimized layer images.

4.3.4 System implementation and experimental results

The light field display was implemented for the real-time 3D visualization of living cells with dual-dimensional imaging system. Figure 4.22 shows the implemented light field display system. Two 22-inch IPS-LCD monitors (LG-22MP57HQ-P) were utilized and the panels are stacked with the precise lateral and angular alignment. The gap was set to 12 mm with the spacer. The detailed specification of the light field display is listed in Table 4.3. Figure 4.22 shows the implemented light field display system for dual-dimensional imaging system.

Table 4.3 Specifications of the implemented light field display system.

22-inch LCD monitor	Pixel pitch	254 μm
	Resolution	1920 \times 1080
gap		12 mm
Maximum viewing angle		12.19 $^\circ$
Number of sampled light fields		5 \times 5

Figure 4.23 shows the experimental results of the 3D visualization of *c.elegans* images with the implemented light field display. The images at the right column are the captured images with a camera. The captured raw images provided the horizontal and vertical parallax as expected. However, the resultant images had higher contrast than the simulation. It is because of the gamma value of the LCD monitor, and can be corrected with the simple pre-processing. However, the gamma correction was not applied in the

system because the additional pre-processing increases the time cost and the higher contrast is usually preferred for the vivid visualization.

With the implemented system, the 3D video of living cells could be observed through the light field display in real-time. Figure 4.24 shows the experimental result of the perspective view videos of moving *c.elegans*. The experimenter can observe the 3D behavior of living cells with the system, and can obtain the view videos from the arbitrary viewpoint after the recording. The experimental results show that the proposed real-time 3D visualization system based on dual-dimensional imaging and light field display can provide 3D images of living cells in real-time with a higher resolution compared to the previous studies.

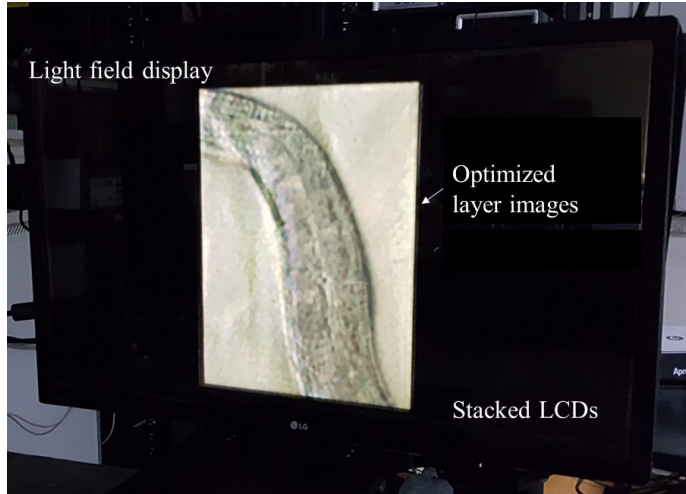


Figure 4.22 The implemented light field display system for dual-dimensional imaging system.

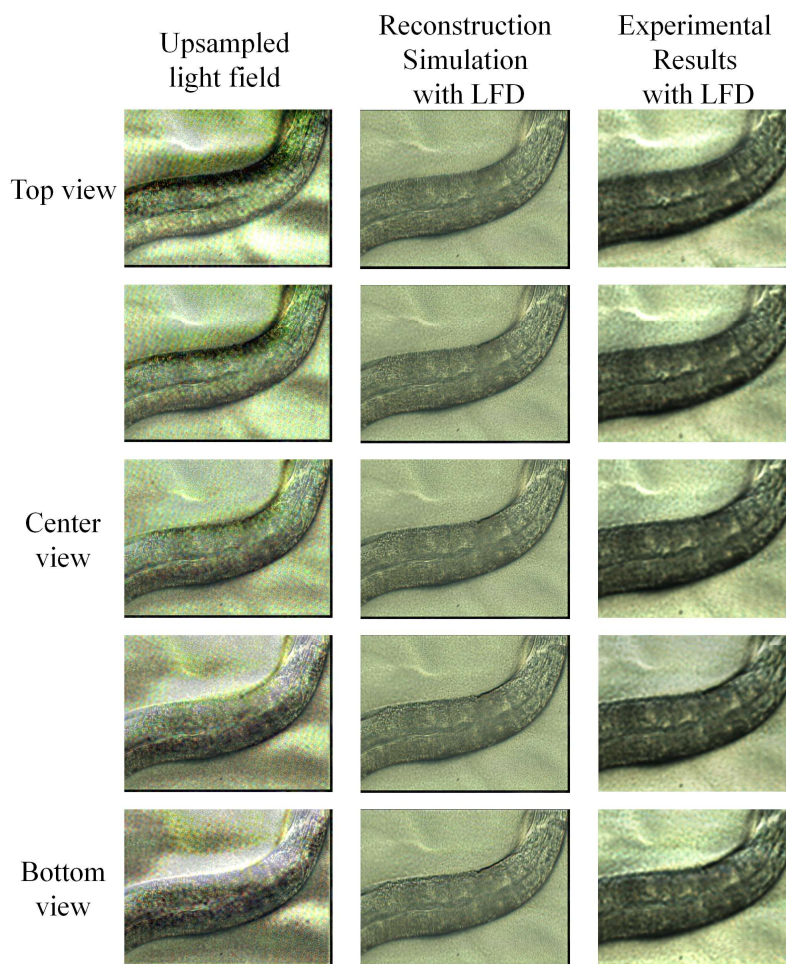


Figure 4.23 The experimental results of 3D visualization of c.elegans with light field display: reconstructed perspective view images of (left) upsampled light field from dual-dimensional imaging, (center) reconstruction simulation of light field display and (right) experimental results with implemented light field display system.

4.4 Conclusion

In this chapter, the real-time 3D visualization method for living cells was proposed based on dual-dimensional imaging and light field display. The dual-dimensional imaging system captured 2D and light field image simultaneously using a beam splitter inside a light field microscope. The light field was upsampled from the captured 2D and light field image based on the Fourier slice photography theorem in real-time. The upsampled light field provided perspective view images with a higher lateral resolution compared to conventional light field microscope. The view video was generated from the upsampled light field sequences obtained by implemented dual-dimensional imaging system.

In addition, the upsampled light field could be visualized in 3D with a light field display. A computational light field display was implemented with two stacked IPS-LCDs. The frontal and rear layer images were optimized in real-time to provide the upsampled light fields from dual-dimensional imaging. The light field upsampling and the layer image optimization algorithm were implemented in parallel for the real-time 3D visualization. The implemented dual-dimensional imaging system and light field display provided 3D images of living cells in real-time with higher resolution compared to previous studies.

Chapter 5 . Conclusion

Previously, the 3D display studies mainly have focused on the improvement of viewing characteristics, so the real-time 3D visualization methods have not been discussed much. In this dissertation, a real-time 3D visualization method was proposed based on light field imaging and light field display. The 3D information was obtained with light field imaging and light field microscope systems and converted to the elemental images for the integral imaging system or layer images for the light field display system. Several approaches were also presented to enhance the resolution in light field imaging.

In chapter 2, a new f-number matching method in light field microscopy was proposed using an elastic PDMS micro lens array. The proposed elastic PDMS micro lens array fabrication method not only was fast and low cost but also could replicate various types of micro lens arrays in a room temperature condition with a precise estimation of the output lens pitch and focal length. The fabricated elastic micro lens array could change its f-number up to 27.3% with the 2D stretching device and could be applied to the multiple objective lenses in the light field microscope system. The results verified that the proposed method can reduce the form factor and the cost of the light field microscope system, and this work would help to give a deeper understanding of elastic micro lens array fabrication and its strain response.

In chapter 3, the real-time elemental image generation algorithm and the real-time 3D visualization systems for the real-scale and the micro-scale

were presented. The integral imaging system could provide the real and orthoscopic 3D images by rearranging the pixel values of the captured images. Based on the algorithm, the system could provide a real-time 3D images of a real-scale objects using a lens array pickup system and an integral imaging system. In addition, the real-time 3D images of a micro-scale objects could be reconstructed in real-time using a light field microscope and an integral imaging system. The depth plane adjustment method and the f-number matching problems in the systems were analyzed to provide 3D images in the best quality. The simulation results and the experimental results were presented to verify the idea.

In chapter 4, the real-time 3D visualization method for living cells was proposed based on dual-dimensional imaging and light field display. The dual-dimensional imaging system captured 2D and light field image simultaneously using a beam splitter inside a light field microscope. The light field could be upsampled from the captured 2D and light field image based on the Fourier slice photography theorem in real-time. The upsampled light field provided perspective view images with a higher lateral resolution compared to conventional light field microscope. The view video was also generated from the upsampled light field sequences obtained by implemented dual-dimensional imaging system.

In addition, the upsampled light field was visualized in 3D with a light field display. A computational light field display was implemented with two stacked IPS-LCDs. The frontal and rear layer images were optimized in real-time to provide the upsampled light fields from the dual-dimensional imaging. The light field upsampling and the layer image optimization

algorithm were implemented in parallel with CUDA for the real-time 3D visualization. The implemented dual-dimensional imaging system and light field display provided 3D images of living cells in real-time with a higher resolution compared to previous studies.

To the best of my knowledge, this dissertation was the first attempt to implement real-time 3D visualization method to observe the real-scale and micro-scale moving objects. Furthermore, the dual-dimensional imaging method was firstly introduced in this dissertation to achieve high resolution light field images in one-shot, and to visualize them in real-time via computational light field display systems. It was also the first approach to fabricate an elastic micro lens array for the light field microscope and apply it to match the f-numbers.

The proposed technologies in this dissertation can be directly applied in various fields. Firstly, the real-time 3D visualization system for the real-scale objects based on the light field imaging and integral imaging can be directly used as a real-time 3D broadcasting system. The proposed real-time elemental image generation algorithm could be practically utilized with the commercialized light field cameras and the integral imaging displays [83, 84].

Secondly, the real-time 3D visualization system for the microscopic objects can be applied in the biomedical imaging. As presented in this dissertation, the observation of the behavior of *c.elegans* has an important meaning in neuroscience fields [66]. The proposed system is helpful to analyze the 3D movement of *c.elegans* such as nictation.

Thirdly, the 3D endoscope is another powerful application of the real-

time 3D visualization system. Compared to the stereoscopic 3D endoscope, the light field imaging system uses one main lens only which can reduce the total radius [85]. The clinical doctors can observe the 3D structure of the internal organs in 3D, in real-time, and without any glasses. The higher resolution with the dual-dimensional imaging system always provides further information.

Since this dissertation focused on the real-time 3D visualization of the micro objects with a high resolution, the theoretical limitation of the axial and lateral resolution was not fully analyzed. Especially, it was worth to verify the resolution enhancement of the 3D deconvolution methods for the dual-dimensional imaging system. I believe that the reconstructed 3D scene with the dual-dimensional imaging system has better quality, but did not prove it through this dissertation. Theoretical analysis as well as the simulations and experiments will be helpful to understand the dual-dimensional imaging systems.

Bibliography

1. J.-M. Chauvet, E. B. Deschamps, and C. Hillaire, *The Dawn of Art: the Chauvet Cave, the Oldest Known Paintings in the World* (Abrams, 1996).
2. H. Rheingold, *Virtual Reality: Exploring the Brave New Technologies* (Simon & Schuster Adult Publishing Group, 1991).
3. A. Patney, J. Kim, M. Salvi, A. Kaplanyan, C. Wyman, N. Benty, A. Lefohn, and D. Luebke, “Perceptually-based foveated virtual reality,” *ACM SIGGRAPH 2016 Emerging Technologies*, Anaheim, California, 2016, 17.
4. W. C. Wiley and I. H. McLaren, “Time-of-flight mass spectrometer with improved resolution,” *Rev. Sci. Instrum.* **26**, 1150 (1955).
5. E.-H. Kim, J. Hahn, H. Kim, and B. Lee, “Profilometry without phase unwrapping using multi-frequency and four-step phase-shift sinusoidal fringe projection,” *Opt. Express* **17**, 7818 (2009).
6. M. Kawakita, K. Iizuka, H. Nakamura, I. Mizuno, T. Kurita, T. Aida, Y. Yamanouchi, H. Mitsumine, T. Fukaya, H. Kikuchi, and F. Sato, “High-definition real-time depth-mapping TV camera: HDTV Axi-Vision Camera,” *Opt. Express* **12**, 2781 (2004).
7. W. J. Matusik and H. Pfister, “3D TV: a scalable system for real-time acquisition, transmission, and autostereoscopic display of dynamic scenes,” *ACM Trans. Graphics* **23**, 814 (2004).
8. F. Okano, H. Hoshino, J. Arai, and I. Yuyama, “Real-time pickup method for a three-dimensional image based on integral photography,” *Appl. Opt.*

- 36**, 1598 (1997).
9. J.-H. Jung, K. Hong, G. Park, I. Chung, J.-H. Park, and B. Lee, “Reconstruction of three-dimensional occluded object using optical flow and triangular mesh reconstruction in integral imaging,” *Opt. Express* **18**, 26373 (2010).
 10. R. Ng, M. Levoy, M. Bredif, G. Duval, M. Horowitz, and P. Hanrahan, “Light field photography with a hand-held plenoptic camera,” Stanford Tech. Rep. CTSR 2005-02 (Stanford University, 2005).
 11. M. Levoy, R. Ng, A. Adams, M. Footer, and M. Horowitz, “Light field microscopy,” *ACM Trans. Graphics* **25**, 924 (2006).
 12. M. Levoy, Z. Zhang, and I. McDowell, “Recording and controlling the 4D light field in a microscope using microlens arrays,” *Journal of Microscopy* **235**, 144 (2009).
 13. M. Broxton, L. Grosenick, S. Yang, N. Cohen, A. Andalman, K. Deisseroth, and M. Levoy, “Wave optics theory and 3-D deconvolution for the light field microscope,” *Opt. Express* **21**, 25418 (2013).
 14. Y. T. Lim, J. H. Park, K. C. Kwon, and N. Kim, “Resolution-enhanced integral imaging microscopy that uses lens array shifting,” *Opt. Express* **17**, 19253 (2009).
 15. A. Orth and K. Crozier, “Microscopy with microlens arrays: high throughput, high resolution and light-field imaging,” *Opt. Express* **20**, 13522 (2012).
 16. J.-H. Park, S.-W. Min, S. Jung, and B. Lee, “Analysis of viewing parameters for two display methods based on integral photography,” *Appl. Opt.* **40**, 5217 (2001).

17. Y.-T. Lim, J.-H. Park, K.-C. Kwon, and N. Kim, "Analysis on enhanced depth of field for integral imaging microscope," *Opt. Express* **20**, 23480 (2012).
18. B. Lee, "Three-dimensional displays, past and present," *Phys. Today* **66**, 36 (2013).
19. W. J. Tam, F. Speranza, S. Yano, K. Shimono, and H. Ono, "Stereoscopic 3D-TV: visual comfort," *IEEE T. Broadcast.* **57**, 335 (2011).
20. B. Javidi and F. Okano, eds., *Three Dimensional Television, Video, and Display Technology* (Springer, 2002).
21. J. Hong, Y. Kim, H.-J. Choi, J. Hahn, J.-H. Park, H. Kim, S.-W. Min, N. Chen, and B. Lee, "Three-dimensional display technologies of recent interest: principles, status, and issues," *Appl. Opt.* **50**, H87 (2011).
22. M. Levoy and P. Hanrahan, "Light field rendering," *ACM SIGGRAPH 1996*, New Orleans, Louisiana, 1996, 31.
23. E. B. Goldstein, *Sensation and Perception* (Cengage Learning, 2013), 9th ed.
24. S. Nagata, "How to reinforce perception of depth in single two-dimensional pictures," in *Pictorial Communication in Virtual and Real Environments* (Tyler & Francis, 1991).
25. J. Kim, Y. Kim, J. Hong, G. Park, K. Hong, S.-W. Min, and B. Lee, "A full-color anaglyph three-dimensional display system using active color filter glasses," *J. Inf. Disp.* **12**, 37 (2011).
26. F. A. Miles, S. J. Judge, and L. M. Optican, "Optically induced changes in the couplings between vergence and accommodation," *J. Neurosci.* **7**, 2576 (1987).

27. J. Kim, J.-Y. Hong, K. Hong, H. K. Yang, S. B. Han, J.-M. Hwang, and B. Lee, "Glasses-free randot stereotest," *J. Biomed. Opt.* **20**, 065004 (2015).
28. J. Kim, H. K. Yang, Y. Kim, B. Lee, and J.-M. Hwang, "Distance stereotest using a 3-dimensional monitor for adult subjects," *Am. J. of Ophthalmol.* **151**, 1081 (2011).
29. S. B. Han, H. K. Yang, J. Kim, K. Hong, B. Lee, J.-M. Hwang, "New Stereoacuity Test Using a 3-Dimensional Display System in Children," *PLOS One* **10**, e0116626 (2015).
30. J.-Y. Son, W.-H. Son, S.-K. Kim, K.-H. Lee, and B. Javidi, "Three-dimensional imaging for creating real-world-like environments," *Proc. IEEE* **101**, 190 (2013).
31. Y. Takaki and N. Nago, "Multi-projection of lenticular displays to construct a 256-view super multi-view display," *Opt. Express* **18**, 8824 (2010).
32. J.-H. Lee, J. Park, D. Nam, S.Y. Choi, D.-S. Park, and C.Y. Kim, "Optimal projector configuration design for 300-Mpixel multi-projection 3D display," *Opt. Express* **21**, 26820 (2013).
33. J.-H. Jung, J. Yeom, J. Hong, K. Hong, S.-W. Min, and B. Lee, "Effect of fundamental depth resolution and cardboard effect to perceived depth resolution on multi-view display," *Opt. Express* **19**, 20468 (2011).
34. J.-Y. Son, V. V. Saveljev, J.-S. Kim, K.-D. Kwack, and S.-K. Kim, "Multiview image acquisition and display," *J. Disp. Technol.* **2**, 359 (2006).
35. G. Lippmann, "La photographie integrale," *Comptes Rendus Acad. Sci.*,

- Paris, C. R. **146**, 446 (1908).
36. J.-H. Park, K. Hong, and B. Lee, "Recent progress in three-dimensional information processing based on integral imaging," *Appl. Opt.* **48**, H77 (2009).
 37. J. Hong, Y. Kim, H.-J. Choi, J. Hahn, J.-H. Park, H. Kim, S.-W. Min, N. Chen, and B. Lee, "Three-dimensional display technologies of recent interest: principles, status, and issues," *Appl. Opt.* **50**, H87 (2011).
 38. S.-g. Park, J. Yeom, Y. Jeong, N. Chen, J.-Y. Hong, and B. Lee, "Recent issues on integral imaging and its applications," *J. Inf. Disp.* **15**, 37 (2014).
 39. Y. Kim, K. Hong, J. Yeom, J. Hong, J.-H. Jung, Y. W. Lee, J.-H. Park, and B. Lee, "A frontal projection-type three-dimensional display," *Opt. Express* **20**, 20130 (2012).
 40. G. Wetzstein, D. Lanman, W. Heidrich, and R. Raskar, "Layered 3D: tomographic image synthesis for attenuation-based light field and high dynamic range displays," *ACM Trans. Graph.* **30**, 95 (2011).
 41. D. Lanman, G. Wetzstein, M. Hirsch, W. Heidrich, and R. Raskar, "Polarization fields: dynamic light field display using multi-layer LCDs," *ACM Trans. Graph.* **30**, 186 (2011).
 42. F. Huang, K. Chen, and G. Wetzstein, "The light field stereoscope: immersive computer graphics via factored near-eye light field displays with focus cues," *ACM Trans. Graph.* **33**, 60 (2015).
 43. S. Lee, C. Jang, S. Moon, J. Cho, and B. Lee, "Additive light field displays: realization of augmented reality with holographic optical elements," *ACM Trans. Graph.* **35**, 60 (2016).

44. G. Wetzstein, D. Lanman, M. Hirsch, and R. Raskar, "Tensor displays: compressive light field synthesis using multilayer displays with directional backlighting," *ACM Trans. Graph.* **31**, 1 (2012).
45. J. Kim, J.-H. Jung, C. Jang, and B. Lee, "Real-time capturing and 3D visualization method based on integral imaging," *Opt. Express* **21**, 18742 (2013).
46. J. Kim, J.-H. Jung, Y. Jeong, K. Hong, and B. Lee, "Real-time integral imaging system for light field microscopy," *Opt. Express* **22**, 10210 (2014).
47. J. Kim, Y. Jeong, H. Kim, C.-K. Lee, B. Lee, J. Hong, Y. Kim, Y. Hong, S.-D. Lee, and B. Lee, "F-number matching method in light field microscopy using an elastic micro lens array," *Opt. Lett.* **41**, 2751 (2016).
48. J.-H. Jung, J. Kim, and B. Lee, "Solution of pseudoscopic problem in integral imaging for real-time processing," *Opt. Lett.* **38**, 76 (2013).
49. B. Javidi, S. Yeom, I. Moon, and M. Daneshpanah, "Real-time automated 3D sensing, detection, and recognition of dynamic biological micro-organic events," *Opt. Express* **14**, 3806 (2006).
50. M. Martínez-Corral, B. Javidi, R. Martínez-Cuenca, and G. Saavedra, "Formation of real, orthoscopic integral images by smart pixel mapping," *Opt. Express* **13**, 9175 (2005).
51. J. Arai, F. Okano, H. Hoshino, and I. Yuyama, "Gradient-index lensarray method based on real-time integral photography for three-dimensional images," *Appl. Opt.* **37**, 2034 (1998).
52. Y. Jeong, J. Kim, J. Yeom, C.-K. Lee, and B. Lee, "Real-time depth controllable integral imaging pickup and reconstruction method with a

- light field camera,” *Appl. Opt.* **54**, 10333 (2015).
53. A. Cattoni, A.-M. Haghiri-Gosnet, D. Decanini, J. Shi, and J. Chen, *Soft UV Nanoimprint Lithography: A Versatile Tool for Nanostructuring at the 20 nm Scale* (InTech, 2011).
 54. L. Desmet, S. Van Overmeire, J. Van Erps, H. Ottevaere, C. Debaes, and H. Thienpont, “Deep proton writing: a powerful rapid prototyping technology for various micro-optical components,” *J. Micromech. Microeng.* **17**, 81 (2006).
 55. Y. M. Song, Y. Xie, V. Malyarchuk, J. Xiao, I. Jung, K.-J. Choi, Z. Liu, H. Park, C. Lu, R.-H. Kim, R. Li, K. B. Crozier, Y. Huang, and J. A. Rogers, “Digital cameras with designs inspired by the arthropod eye,” *Nature* **497**, 95 (2013).
 56. D. Hoheisel, C. Kelb, M. Wall, B. Roth, and L. Rissing, “elastomeric PDMS planoconvex lenses fabricated by a confined sessile drop technique,” *J. Eur. Opt. Soc.* **8**, 13065 (2013).
 57. D. Chandra, S. Yang, and P.-C. Lin, “Strain responsive concave and convex microlens arrays,” *Appl. Phys. Lett.* **91**, 251912 (2007).
 58. H. Kim, J. Kim, J. Kim, B. Lee, and S.-D. Lee, “Liquid crystal-based lenticular lens array with laterally shifting capability of the focusing effect for autostereoscopic displays,” *Opt. Commun.* **357**, 52 (2015).
 59. H. Hassanin and K. Jiang, “Multiple replication of thick PDMS micropatterns using surfactants as release agents,” *Microelectron. Eng.* **88**, 3275 (2011).
 60. T.-K. Shin, J.-R. Ho, and J.-W. Cheng, “A new approach to polymeric microlens array fabrication using soft replica molding,” *IEEE Photon.*

- Technol. Lett. **16**, 2078 (2004).
61. Y. Kim, K. Hong, J. Yeom, J. Hong, J.-H. Jung, Y. W. Lee, J.-H. Park, and B. Lee, "A frontal projection-type three-dimensional display," *Opt. Express* **20**, 20130 (2012).
 62. Y. Takaki, Y. Urano, S. Kashiwada, H. Ando, and K. Nakamura, "Super multi-view windshield display for long-distance image information presentation," *Opt. Express* **19**, 704 (2011).
 63. A. Levin, R. Fergus, F. Durand, and T. W. Freeman, "Image and depth from a conventional camera with a coded aperture," *ACM Trans. Graph.* **26**, 70 (2007).
 64. J.-H. Park, Y. Kim, J. Kim, S.-W. Min, and B. Lee, "Three-dimensional display scheme based on integral imaging with three-dimensional information processing," *Opt. Express* **12**, 6020 (2004).
 65. J.-H. Park, M.-S. Kim, G. Baasantseren, and N. Kim, "Fresnel and Fourier hologram generation using orthographic projection images," *Opt. Express* **17**, 6320 (2009).
 66. J.-H. Park, G. Baasantseren, N. Kim, G. Park, J.-M. Kang, and B. Lee, "View image generation in perspective and orthographic projection geometry based on integral imaging," *Opt. Express* **16**, 8800 (2008).
 67. H. Kim, J. Hahn, and B. Lee, "Mathematical modeling of triangle-mesh-modeled three-dimensional surface objects for digital holography," *Appl. Opt.* **47**, D117 (2008).
 68. S. Park, J.-H. Kim, and S.-W. Min, "Polarization distributed depth map for depth-fused three-dimensional display," *Opt. Express* **19**, 4316 (2011).

69. R. Kaptein and I. Heynderickx, "Effect of crosstalk in multi-view autostereoscopic 3D displays on perceived image quality," *SID Symposium Digest of Technical Papers* **38**, 1220 (2007).
70. Y. Kim, J. Yeom, J.-H. Jung, J. Hong, and B. Lee, "View image error analysis based on focal mode and virtual mode in three-dimensional display using lenses," *Proc. SPIE* **7956**, 79560S (2011).
71. Y. Kim, G. Park, J.-H. Jung, J. Kim, and B. Lee, "Color moiré pattern simulation and analysis in three-dimensional integral imaging for finding the moiré-reduced tilted angle of a lens array," *Appl. Opt.* **48**, 2178 (2009).
72. J. Kim, J.-H. Jung, J. Hong, J. Yeom, and B. Lee, "Elemental image generation method with the correction of mismatch error by sub-pixel sampling between lens and pixel in integral imaging," *J. Opt. Soc. Korea* **16**, 29 (2012).
73. E. Betzig and R. J. Chichester, "Single molecules observed by near-field scanning optical microscopy," *Science* **262**, 1422 (1993).
74. A. Fire, S. Xu, M. K. Montgomery, S. A. Kostas, S. E. Driver, and C. C. Mello, "Potent and specific genetic interference by double-stranded RNA in *Caenorhabditis elegans*," *Nature* **391**, 806 (1998).
75. H. Lee, M. K. Choi, D. Lee, H. S. Kim, H. Hwang, H. Kim, S. Park, Y. K. Paik, and J. Lee, "Nictation, a dispersal behavior of the nematode *Caenorhabditis elegans*, is regulated by *il2* neurons," *Nat. Neurosci.* **15**, 107 (2011).
76. M. Ben Ezra, E. Boyden, C. Rowlands, and Y.-G. Yoon, "Methods and apparatus for stretched light field microscope." U.S. Patent No.

- 20,160,091,705, (2016).
77. C. H. Lu, S. Muenzel, and J. Fleischer, “High-resolution light-field microscopy,” in *Computational Optical Sensing and Imaging, Microscopy and Tomography I (CTh3B)*, Arlington, 2013, 2.
 78. R. Ng, “Fourier slice photography,” *ACM Trans. Graph.* **24**, 735 (2005).
 79. J.-H. Park, S.-K. Lee, N.-Y. Jo, H.-J. Kim, Y.-S. Kim, and H.-G. Lim, “Light ray field capture using focal plane sweeping and its optical reconstruction using 3D displays,” *Opt. Express* **22**, 25444 (2014).
 80. V. Podlozhnyuk, “FFT-based 2D convolution.” NVIDIA white paper 32 (2007).
 81. J. L. Jodra, I. Gurrutxaga and J. Muguerza, “A Study of Memory Consumption and Execution Performance of the cuFFT Library,” in *2015 10th International Conference on P2P, Parallel, Grid, Cloud and Internet Computing (3PGCIC)*, Krakow, 2015, 323.
 82. D. Lanman, M. Hirsch, Y. Kim, and R. Raskar, “Content-adaptive parallax barriers: optimizing dual-layer 3D displays using low-rank light field factorization,” *ACM Trans. Graph.* **29**, 163 (2010).
 83. <https://www.lytro.com/>
 84. <https://www.raytrix.de/>
 85. N. Taffinder, S. G. T. Smith, J. Huber, R. C. G. Russell, and A. Darzi, “The effect of a second-generation 3D endoscope on the laparoscopic precision of novices and experienced surgeons,” *Surg. Endosc.* **13**, 1087 (1999).

Appendix

Portions of the work discussed in this dissertation are also presented in the following publications:

[Chapter 2] J. Kim, Y. Jeong, H. Kim, C.-K. Lee, B. Lee, J. Hong, Y. Kim, Y. Hong, S.-D. Lee, and B. Lee, “F-number matching method in light field microscopy using an elastic micro lens array,” *Opt. Lett.* **41**, 2751 (2016).

[Chapter 3.2] J.-H. Jung, J. Kim, and B. Lee, “Solution of pseudoscopic problem in integral imaging for real-time processing,” *Opt. Lett.* **38**, 76 (2013).

[Chapter 3.3] J. Kim, J.-H. Jung, C. Jang, and B. Lee, “Real-time capturing and 3D visualization method based on integral imaging,” *Opt. Express* **21**, 18742 (2013).

[Chapter 3.4] J. Kim, J.-H. Jung, Y. Jeong, K. Hong, and B. Lee, “Real-time integral imaging system for light field microscopy,” *Opt. Express* **22**, 10210 (2014).

초 록

본 박사학위 논문에서는 라이트 필드 이미징 (light field imaging) 기술을 이용하여 실시간으로 3차원 시각화를 하는 방법을 제안한다. 라이트 필드 이미징 기술은 카메라 센서 앞의 렌즈 어레이를 이용해 한 번의 촬영으로 3차원 정보를 얻을 수 있다. 본 논문에서는 라이트 필드 이미징 시스템을 이용하여 얻은 3차원 정보를 실시간으로 집적영상 시스템으로 재생하는 방법을 제안한다. 다시점 기초 영상 (base image) 획득 알고리즘에 기반하여 집적영상을 위한 실시간 요소 영상 (elemental image) 획득 알고리즘을 개발한다. 이 알고리즘은 필요에 따라 재생 깊이 면을 조절할 수 있고, 3차원 장면에 따라 실상과 허상을 함께 재생할 수 있다. 제안된 시스템은 실제 크기의 물체를 실시간으로 3차원 공간에 재생할 수 있고, 이는 실시간 방송 등의 기술에 적용될 수 있다.

라이트 필드 이미징에 기반한 실시간 3차원 시각화 방법을 확장하여, 라이트 필드 현미경 (light field microscope) 에 적용한다. 라이트 필드 현미경을 통해 얻은 미세 물체의 3차원 정보를 집적영상 시스템으로 재생할 수 있다. 요소영상은 비슷한 실시간 알고리즘을 이용해 획득할 수 있다. 이 때, 대물렌즈와 재생 렌즈 어레이의 f 수 (f -number)를 고려하여 요소영상을 제작하여야 한다. 제안된 방법을 라이트 필드 현미경과 집적영상 시스템을 제작하여 검증한다. 이 시스템은 살아있는 세포의 3차원 움직임을 추적하며 관찰할 수 있다.

한편, 라이트 필드 이미징은 카메라 센서 앞 마이크로 렌즈어레이 때문에 태생적인 해상도 한계를 갖는다. 이에 이중차원 이미징 (dual-dimensional imaging) 방법을 제안한다. 이중차원 이미징은 광경로 내부의 반거울을 이용하여 물체의 2차원 이미지와 라이트필드 이미지를 동시에 획득하는 방법이다. 얻어낸 두 영상은 푸리에 조각 사진 이론 (Fourier slice photography theorem)에 기반하여 업샘플링 (upsampling) 된 라이트 필드로 변환 가능하다. 라이트 필드 현미경 내부의 반거울을 이용하여 이중차원 이미징 시스템을 제작하고, 얻어낸 라이트 필드를 기존 라이트 필드 현미경과 비교하여 검증한다.

이중차원 이미징에서 얻어낸 고해상도 라이트 필드를 계산형 라이트 필드 디스플레이 (computational light field display)로 실시간으로 3차원 시각화 한다. 이 때 라이트필드 업샘플링과 라이트 필드 디스플레이의 층 이미지는 병렬 연산을 이용해 실시간으로 제작한다. 두 장의 액정 디스플레이를 포개서 제작한 라이트 필드 디스플레이로 이중 차원 이미징으로 얻어낸 고해상도 라이트 필드를 실시간으로 재생할 수 있다.

또한, 라이트 필드 현미경에서 다양한 대물렌즈에 적용될 수 있는 탄성적인 마이크로 렌즈 어레이를 제작한다. 라이트 필드 현미경에서 최대 해상도를 얻기 위해서는 대물렌즈와 마이크로 렌즈 어레이의 f 수가 일치해야 해서, 대물렌즈마다 마이크로 렌즈 어레이가 짝지어져야 한다. 탄성적인 마이크로 렌즈 어레이는 당기는 힘에 따라 f 수가 달라지기 때문에 다양한 종류의 대물렌즈에 적용가능하다. 폴리디메틸실록산 (PDMS)를 이용하여 기존 마이크로 렌즈어레이의 주물을 제작하고 이를 이용하여

탄성적인 폴리디메틸실록산 마이크로 렌즈 어레이를 얻어낸다. 얻어낸 탄성 마이크로 렌즈 어레이로 라이트 필드 현미경을 구성하여 검증한다.

기존 3차원 디스플레이 연구는 대부분 디스플레이 특성을 향상시키는 방향이었기 때문에 실시간 3차원 시각화에 대한 연구는 부족하였다. 본 논문에서는 한 번의 촬영으로 얻은 고해상도 3차원 정보를 다시 3차원 디스플레이를 이용하여 실시간으로 재생하는 방법을 제안한다. 제안된 방법은 향후 3차원 방송 기술이나 3차원 의료 기술 등의 발전에 기여할 수 있을 것으로 기대된다.

주요어: 실시간 3 차원 시각화, 라이트 필드 이미징, 라이트 필드 현미경, f수 매칭, 탄성 마이크로 렌즈 어레이.

학 번: 2011-20814